Journal of Materials Science & Technology 196 (2024) 71–87

Contents lists available at ScienceDirect

Journal of Materials Science & Technology

journal homepage: www.elsevier.com/locate/jmst

Research Article

Unveiling deformation behavior and damage mechanism of irradiated high entropy alloys

Shuo Wang[a], Yang Chen[a], Jia Li[a,*], Bin Liu[b], Ruiqian Zhang[c], Peter K Liaw[d], Qihong Fang[a,*]

[a] State Key Laboratory of Advanced Design and Manufacturing for Vehicle Body, College of Mechanical and Vehicle Engineering, Hunan University, Changsha 410082, China
[b] State Key Laboratory of Powder Metallurgy, Central South University, Changsha 410083, China
[c] Science and Technology on Reactor Fuel and Materials Laboratory, Nuclear Power Institute of China, Chengdu 610213, China
[d] Department of Materials Science and Engineering, The University of Tennessee, Knoxville, TN 37996, USA

ARTICLE INFO

Article history:
Received 12 January 2024
Revised 10 February 2024
Accepted 12 February 2024
Available online 11 March 2024

Keywords:
Oxide dispersion strengthening
High entropy alloy
Radiation
Dislocation
Damage model

ABSTRACT

The oxide dispersion strengthening (ODS) high entropy alloy (HEA) exhibits the high elevated temperature performance and radiation resistance due to severe atomic lattice distortion and oxide particles dispersed in matrix, which is expected to become the most promising structural material in the next generation of nuclear energy systems. However, microstructure and damage evolution of irradiated ODS HEA under loading remain elusive at submicron scale using the existing simulations owing to a lack of atomic-lattice-distortion information from a micromechanics description. Here, the random field theory informed discrete dislocation dynamics simulations based on the results of high-resolution transmission electron microscopy are developed to study the dislocation behavior and damage evolution in ODS HEA considering the influence of severe lattice distortion and nanoscale oxide particle. Noteworthy, the damage behavior shows an unusual trend of the decreasing-to-increasing transition with the continuous loading process. There are two main types of damage micromechanics generated in irradiated ODS HEA: the dislocation loop damage in which the damage is controlled by irradiation-induced dislocation loops and their evolution, the strain localization damage in which the damage comes from the dislocation multiplication in the local plastic region. The oxide particle hinders the dislocation movement in the main slip plane, and the lattice distortion induces the dislocation sliding to the secondary slip plane, which promotes the dislocation cross-slip and dislocation loop annihilation, and thus reduces the material damage in the elastic damage stage. These findings can deeply understand atomic-scale damage mechanism and guide the design of ODS HEA with high radiation resistance.

1. Introduction

Energy has always been the foundation of the development of human society and civilization. However, with the rapid progress in society and the advancement of industrial technology, fossil energy, such as oil and coal which human beings rely on for survival, is declining sharply. Also, the utilization of other renewable energy, such as wind energy, water energy, and solar energy, is not enough to replace fossil energy [1,2]. Therefore, the achievement of societal sustainable development and the preservation of the natural environment have emerged as a significant challenge for humanity in the 21st century [3]. Nuclear energy is a well-established and extensively deployed energy, which is regarded as a pivotal solution to address future energy challenges. However, under the extreme service environment, the performance and life of materials become the key factors restricting the development of nuclear energy and determining the safety of nuclear reactors [4–6]. The structural components of nuclear reactors are exposed to high-energy particle radiation for a long time, resulting in a large number of point defects, such as vacancies and interstitial atoms [7–9]. These point defects migrate and aggregate, leading to the formation of dislocation loops and voids, ultimately causing degradation in the macroscopic properties of the material [10,11].

High entropy alloys (HEAs) are alloys formed by five or more elements with similar contents, which have outstanding mechanical properties, high-temperature properties, and irradiation resistance, thus becoming competitive candidates for key components of nuclear reactors [12–16]. Experimental research demonstrates that HEA exhibits exceptional structural stability under He-ion ir-

* Corresponding authors.
E-mail addresses: lijia123@hnu.edu.cn (J. Li), fangqh1327@hnu.edu.cn (Q. Fang).

https://doi.org/10.1016/j.jmst.2024.02.017
1005-0302/

radiation due to its low mobility of He atoms and point defects [17]. Moreover, transmission electron microscopy (TEM) and electron energy loss spectroscopy (EELS) experiments show that with the increase of the composition complexity of HEAs, the generation of perfect dislocation loops is suppressed [18]. Even HEAs with scarcely irradiation hardening after helium-ion irradiation have been developed. This particular irradiation resistance is attributed to the high-density lattice vacancies and low mobility of point defects [19,20]. Relevant theoretical investigations and simulations have been carried out to elucidate the unique radiation resistance mechanism of HEA [6,21,22]. Molecular dynamics (MD) simulations of the displacement cascade induced by irradiation in NiCoCrFe HEA show that the low thermal conductivity, enhanced thermal spikes, and small binding energies of interstitial loops in NiCoCrFe HEA hinder the heat dissipation, leading to delayed growth of defects in NiCoCrFe-HEA [22]. Based on large-scale MD simulation and TEM with in situ ion irradiation characterization experiments, the presence of chemical short-range ordering is demonstrated to decelerate the formation and evolution of point defects during irradiation [6]. The irradiation hardening of HEAs with severe lattice distortion fields is investigated by discrete dislocation dynamics (DDD) simulations. The severe lattice distortion in HEAs can facilitate the cross-slip of dislocations, leading to a more homogeneous distribution of defect-free channels and consequently enhancing irradiation performance [21]. Based on the above researches, the complex composition, unique lattice distortion, and hysteresis diffusion effects of HEA can effectively suppress the generation of irradiation defects and the degradation of performance.

The oxide dispersion-strengthened alloys with excellent resistance to irradiation and high-temperature creep are one of the priority candidate materials for the first wall/blanket materials in reactors [23–25]. After the He-ion irradiation at high temperatures, the bubbles observed in oxide dispersion strengthening (ODS) steels are smaller than the Fe14Cr alloy, indicating higher radiation resistance of ODS alloys [26]. Furthermore, the TEM analysis of the ODS FeCrNi medium entropy alloy (MEA) reveals that the exceptional radiation resistance can be ascribed to the introduction of high-density oxide nanoparticles, which can act as sinks for radiation-induced defects, disperse the distribution of defects, inhibit the growth of defects and the segregation induced by irradiation [27]. Another study shows that a smaller oxide particle size and higher oxide particle density can lead to greater recombination of irradiation-induced defects and improve the radiation tolerance of ODS alloys [28].

According to the aforementioned works, the excellent resistance to irradiation of HEAs and ODS alloys has been demonstrated. The complex composition, unique lattice distortion, and diffusion hysteretic effect of HEA, as well as the dispersed oxide particles in ODS alloys, can effectively improve the irradiation resistance of the alloys. Therefore, the ODS HEA, which combines the characteristics of these two alloys, is considered to have significant potential for applications in irradiation-intensive environments, such as nuclear reactors [25]. The latest research indicates that the ODS HEAs exhibit excellent irradiation resistance, similar to high-entropy alloys. Moreover, the ODS HEAs have an enhanced intrinsic strength attributed to the existence of ultrafine particles, which impede the movement of dislocations and play the role of dispersion strengthening [29,30]. Although developing ODS HEA with high irradiation resistance through the novel alloying design and microstructure-tailoring has been highly anticipated, relevant irradiation studies typically focus on ODS alloys or HEAs, but very little on ODS HEA [23–30]. Furthermore, the few reports on irradiation of ODS HEAs generally center on the evolution of defects during irradiation, and rarely on the properties of ODS HEAs after irradiation. On the mesoscopic scale, the radiation properties and microscopic mechanisms of ODS HEAs still require further elucidation [31]. The dislocation evolution mechanism under the coupling of oxide particles and lattice distortion field has not been revealed. In addition, it has been widely accepted that the dislocation interacts with oxide particles through the Orowan mechanism [32–34]. However, a large number of recent experiments have shown that the nano-scale oxide particles are coherent or semi-coherent with the matrix, which provides support for the oxide particles cut by the dislocation [35–38]. Therefore, when the oxide particle size is very small, the case of the oxide particle being cut by the dislocation should be considered. In this research, the lattice distortion field of HEAs measured by high-resolution transmission electron microscopy (HRTEM) is embedded into DDD simulation through random field theory to investigate the evolution of large-scale dislocation and irradiation defects during loading in ODS HEAs. The interaction of dislocations with dislocation loops and oxide particles is studied in detail. The stress damage factor is defined to provide a quantitative description of the damage degree during the evolution process. The damage of HEAs and ODS HEAs is compared.

2. Experiment

2.1. Material preparation

The ingot of an equiatomic FeCoCrNi HEA was synthesized by a vacuum-induction melting method. High purity (> 99.9 wt%) elemental metal powders were used as the raw materials for the preparation of the FeCoCrNi HEA. Thoroughly mixed powders of equal molar ratio were placed in an alumina crucible, and then were heated by induction heating in a high-purity argon atmosphere until they were completely melted. The ingot was remelted four times to ensure the uniformity of the various elements and cast into a cylindrical mold with a diameter of 10 mm. Prior to furnace cooling, the ingot was vacuum-sealed and homogenized at 1273 K for 12 h.

2.2. Characterization method

The equiatomic FeCoCrNi HEA samples were cut by electrical discharge machining wire, followed by mechanical polishing into a thickness of about 50 μm with SiC sandpaper. In recent years, many methods have been developed to measure lattice distortion of HEAs, among which HRTEM combined with the geometric phase analysis (GPA) is widely accepted. Here, the HRTEM image of the undeformed FeCoCrNi HEA sample was obtained by a JEOL JEM 2100F microscope.

3. Methodology

3.1. Lattice distortion to DDD

In DDD simulation, dislocation movement is obtained by the integral of node velocities. The velocity of the dislocation node is controlled by the node force and the damping coefficient of the dislocation. The force exerted on the node is obtained by superimposing the segment force connecting to the node according to the contribution [21]:

$$F_i = \sum_j f_{ij} \tag{1}$$

where F_i is the force on the dislocation node i. f_{ij} is the force on the dislocation segment ij, which is obtained from the Peach–Koehler force

$$f_{ij} = \int_{C_j} N_i^j(s) f_{ij}^{\mathrm{PK}}(s) \mathrm{d}L(s) \tag{2}$$

where C_j represent the dislocation segment, d$L(s)$ is the differential of the dislocation segment at location s, N_i^j is the shape function. For node i at location s,

$$N_i^j(s) = s(0 \le s \le 1) \tag{3}$$

here, considering the effect of lattice distortion, the Peach–Koehler force is expressed as

$$f_{ij}^{\mathrm{PK}}(s) = \left[\sigma^{\mathrm{ext}}(s) + \sigma^{\mathrm{disl}}(s) + \sigma^{\mathrm{HEA}}(s)\right] \cdot \boldsymbol{b}_{ij} \times \boldsymbol{t}_{ij} \tag{4}$$

where $\sigma^{\mathrm{ext}}(s)$ is the externally-applied stress, $\sigma^{\mathrm{disl}}(s)$ is the stress from other dislocations, $\sigma^{\mathrm{HEA}}(s)$ is the stress from the lattice distortion, $\boldsymbol{b}_{ij}$ represents the Burgers vector of the dislocation segment ij, $\boldsymbol{t}_{ij}$ represents the magnitude and the direction of the dislocation segment ij.

For face-centered cubic (FCC) Metals, the velocity of the dislocation node is

$$v_i = \frac{f_i}{B\sum_j L_{ij}/2} \tag{5}$$

where B is the drag coefficient, L_{ij} is the length of the dislocation segment.

3.1.1. Strain field from experiment

The lattice image of the FeCoCrNi HEA is shown in Fig. 1(a). The geometric phase analysis of the image was conducted via the open-source program Strain ++. The filtered inverse fast Fourier transformation (FFT) image is shown in Fig. 1(b), indicating that the HRTEM image is from the defect-free region of the FeCoCrNi HEA. Therefore, it can be guaranteed that the lattice strain field obtained based on GPA is completely caused by severe atomic lattice distortion. The alternating sign of normal strain along the $(\bar{1}\bar{1}1)$ direction implies an inhomogeneous strain field.

3.1.2. Fractal function

As one of the core effects in the HEAs, the severe lattice distortion impedes dislocation movement, leading to solid solution strengthening [13,39–41]. The existence of the lattice strain field has an important effect on the properties of HEAs, which acts as a nonnegligible factor in studying the irradiation hardening of HEAs [17,42,43]. The fractal function has the characteristics of continuity, self-affinity, and non-differentiability. The fractal patterns are widely observed in many natural phenomena such as surface topography and precipitation [21,44]. As reported in the experimental work, fractal patterns were observed in the strain map of the AlCrFeCoNi HEA. Therefore, the fractal function is used to describe the random strain field of the HEA in the current study.

A Weierstrass–Mandelbrot (W–M) function is derived from its univariate form [44]:

$$W(\boldsymbol{r}) = \left(\frac{\ln\gamma}{M}\right)^{\frac{1}{2}} \sum_{m=1}^{M}\sum_{n=-\infty}^{\infty} A_m\left[\cos(\phi_{m,n}) - \cos(k_0\gamma^n \vec{\boldsymbol{n}}_m \cdot \boldsymbol{r} + \phi_{m,n})\right](k_0\gamma^n)^{D-4} \tag{6}$$

where $W(\boldsymbol{r})$ is constant on the circles $|\boldsymbol{r}| = cons\tan t$, γ is a frequency density parameter of the strain wave, $M = 50$ represents the number of superposed ridges used to construct the surface, m means from 1 to M, n is the frequency index, a finite value related to the sample size, and A_m is the amplitude of the fractal surface. In this study, $A_m = (2\pi)^{4-D}H^{D-3}$ is used to obtain an isotropic strain field function in a space, because the widely accepted software packages for DDD simulation are based on the isotropic assumption [45,46]. D is the fractal dimension of the surface and H is the strain amplitude. $\phi_{m,n}$ indicates a random phase. $k_0 = 2\pi/L$, represents the wave number, which is related to the sample length and used to scale horizontal variability. L is the sample length selected in the measurement of the strain field. γ is a parameter related to the frequency density of the surface. $\gamma = 1.5$ is set to match the surface flatness and frequency distribution density of the strain field measured by the experiment, $\vec{\boldsymbol{n}}_m$ are unit vectors spaced uniformly over a unit 3D hypersphere.

Based on the above parameters, a strain field function with a fractal pattern is generated as:

$$\varepsilon(\boldsymbol{r}) = H^{D-3}\left(\frac{\ln\gamma}{M}\right)^{\frac{1}{2}} \sum_{m=1}^{M}\sum_{n=0}^{n_{\max}}\left[\cos\left(\phi_{m,n}\right) - \cos\left(\frac{2\pi\gamma^n\vec{\boldsymbol{n}}_m\cdot\boldsymbol{r}}{L} + \phi_{m,n}\right)\right]\left(\frac{\gamma^n}{L}\right)^{D-4} \tag{7}$$

According to Hooke's law, the stress field corresponding to the generated fractal strain field is calculated by $\sigma_{ij} = 2G\varepsilon_{ij} + \lambda\varepsilon_{kk}\delta_{ij}$, where σ_{ij} is the stress tensor, ε_{ij} is the strain tensor, G is the shear modulus and λ is the Lamé constants, ε_{kk} is the trace of the strain tensor, δ_{ij} is the Kronecker delta.

In current work, the fractal dimension and strain amplitude corresponding to the fractal pattern of the experimental strain field are evaluated by the structure function method [47].

3.1.3. Structure function method

The discrete structure function in a space is defined as

$$S(\tau_x, \tau_y) = \left\langle \left(z(x,y) - z(x+\tau_x, y+\tau_y)\right)^2 \right\rangle \tag{8}$$

where $\tau_x = L_{\mathrm{hori}}\cos\theta$ and $\tau_y = L_{\mathrm{hori}}\sin\theta$ indicate the horizontal and vertical spaces lag between the point (x, y) and

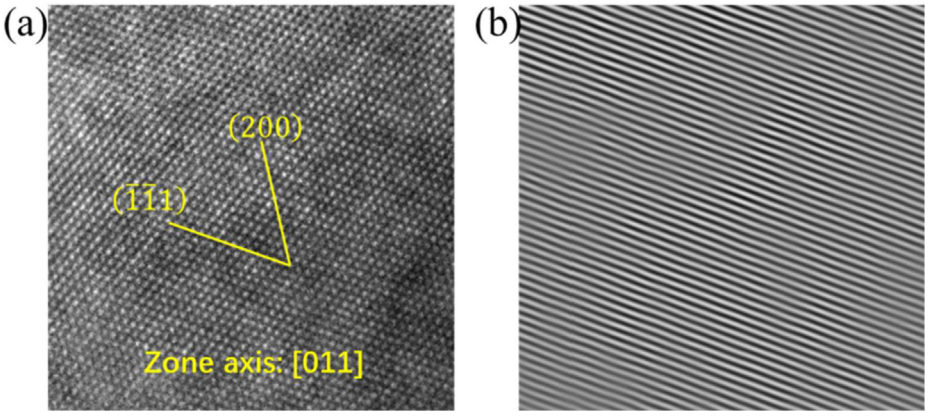

Fig. 1. (a) The high-resolution transmission electron microscopy (TEM) image with the [011] zone axis. (b) The corresponding filtered inverse FFT image of $(\bar{1}\bar{1}1)$ plane.

Table 1
The fractal dimension and strain amplitude of the fractal strain field calculated by the structure function method.

Strain components	ε_{xx}	ε_{yy}	ε_{zz}	$\varepsilon_{xy}\varepsilon_{xy}$	ε_{xz}	ε_{yz}
Fractal dimension	D_{xx} 3.8142	D_{yy} 3.8142	D_{zz} 3.8142	D_{xy} 3.8226	D_{xz} 3.8226	D_{yz} 3.8226
Strain amplitude ($\times 10^{-4}$)	H_{xx} 15.8212	H_{yy} 15.8212	H_{zz} 15.8212	H_{xy} 10.9417	H_{xz} 10.9417	H_{yz} 10.9417

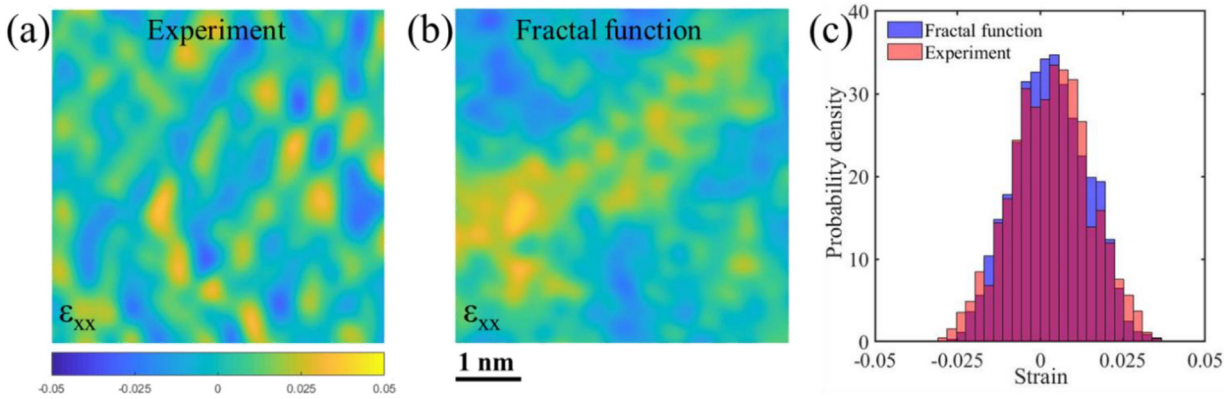

Fig. 2. The contour map of the normal lattice strain field obtained by (a) the experiment and (b) the fractal function. (c) The statistical distributions of the normal residual strain obtained by the experiment and fractal function.

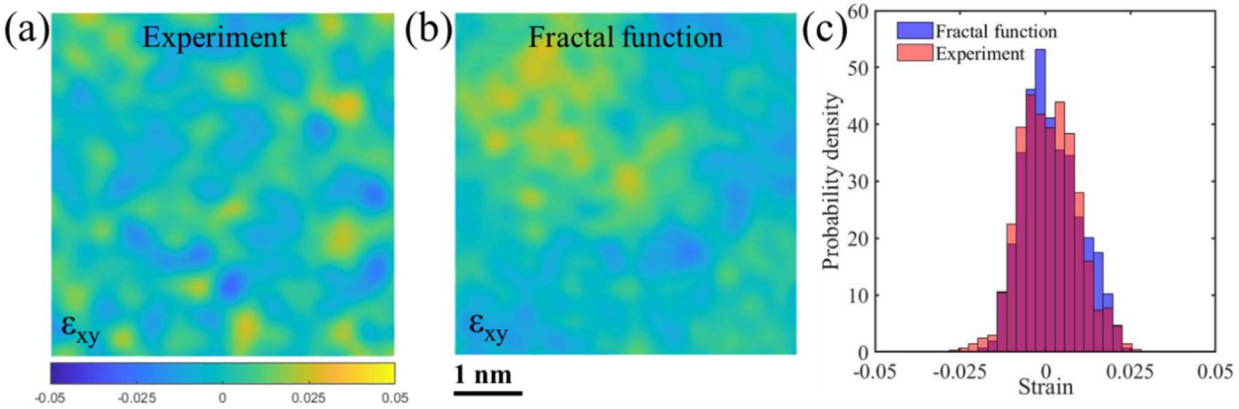

Fig. 3. The contour map of the shear lattice strain obtained by (a) the experiment and (b) the fractal function. (c) The statistical distributions of the shear residual strain obtained by the experiment and fractal function.

$(x+\tau_x, y+\tau_y)$, L_{hori} indicates the horizontal distance between two points, $\langle \ldots \rangle$ means to take the spatial average value, and $z(x,y)$ is the strain at point (x,y) characterized by experiment. θ is used to construct a corresponding number of profiles from the image which represents 50 evenly distributed discrete values between 0 and 2π. It is assumed that the structure function profiles derived from the images obey the approximate scale-law behavior:

$$S(L_{\text{hori}}) = \Lambda (L_{\text{hori}})^{2(2-D_s)} \tag{9}$$

where $D_s = (4 - T_s)/2$ is the fractal dimension of profiles derived from the images, T_s is the slope of the log-log graph of S and L_{hori}, and $\ln(\Lambda)$ is the intercept. The fractal dimension, D_s is calculated from the above equation. The strain amplitude is calculated by:

$$H = \left[-\frac{2}{\pi} \Lambda \Gamma (5 - 2D_s) \sin (\pi D_s) \right]^{1/(2D_s - 2)} \tag{10}$$

where $\Gamma(x)$ is the gamma function.

The fractal dimension of the strain field is computed according to:

$$D = \langle D_s \rangle + 2 \tag{11}$$

The fractal dimension and strain amplitude calculated by the structural function method and experiment are listed in Table 1.

Fig. 2 shows the comparison of the fractal normal residual strain field and the experimental normal residual strain field. The statistical distributions of the normal residual strain field show a good agreement (Fig. 2(c)). It indicates the fractal strain field effectively reflects the characteristics of the experimental strain field (Figs. 2 and 3).

3.2. Dislocation mobility model

The Eshelby–Olmsted approach is selected to describe the dislocation velocity of the FeCoCrNi HEA in the present study. When the velocity of a dislocation is smaller than the critical velocity, only a linear damping term is considered. When the velocity of the dislocation is larger than the critical velocity, a nonlinear damping term is added to the linear term, due to the damping effect caused by the ultrasonic wave emission. The relationship between the shear force and dislocation velocity is written as a phenomeno-

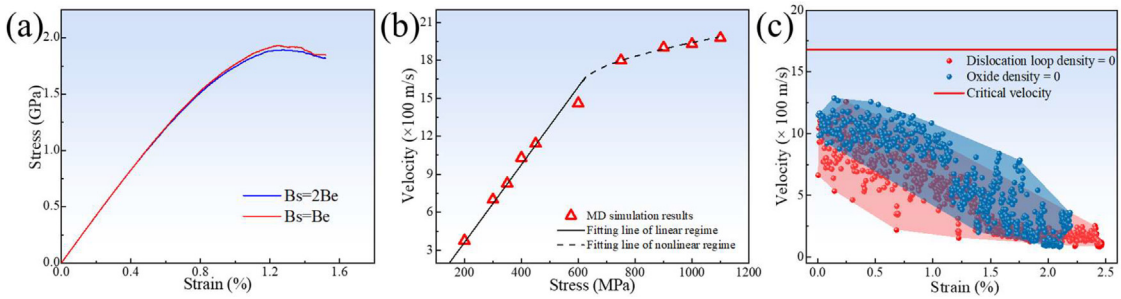

Fig. 4. (a) Stress–strain curves for different drag coefficients of screw/edge dislocation. (b) Dislocation velocity vs. applied stress of an edge dislocation. (c) The dislocation node velocity in DDD simulation.

logical function:

$$\tau b = \begin{cases} B(T)v & v \le v_0 \\ B(T)v + D_n(v - v_0)^{\alpha} & v > v_0 \end{cases} \tag{12}$$

where b is the magnitude of the Burgers vector, τ is the applied shear force, B is the linear damping coefficient in relation to the temperature, T is the temperature, v is the dislocation velocity, v_0 is the critical velocity, D_n is the drag coefficient of the nonlinear term, and α is the nonlinear power law exponent.

Recent studies have reported that the MD simulation results show a little difference in the mobility between screw and edge dislocations in the FeCoCrNiCu HEA [48]. Therefore, we used different drag coefficients of screw/edge dislocations to conduct DDD simulations to investigate the influence of dislocation mobility. The simulation results in Fig. 4(a) indicate that although the drag coefficient of the screw dislocation is doubled, there is little change in the stress–strain curve. These results indicate that in DDD simulation, different mobility for screw/edge dislocation will hardly cause changes in the stress–strain curve [49]. Therefore, in the current DDD simulation, screw and edge dislocations are considered to have the same drag coefficient, which is consistent with other recent DDD studies [20,50]. In order to determine the drag coefficient of the dislocation, we perform DDD simulation and calculate the velocity of the dislocation with linear drag coefficient (Fig. 4(b)). Considering the preventing effect of oxide particles and dislocation loops on dislocation motion, samples without dislocation loops and oxide particles are selected to calculate the node velocity. It is found that the dislocation velocity is much smaller than that of the nonlinear damping region (Fig. 4(c)). According to the velocity of the dislocation node, the dislocation segment moves in the linear damping region. By fitting the MD simulation results using Eq. (7), the linear damping coefficient in the present study is calculated as 8.149 $\times$ 10^{-5} Pa s at room temperature (Fig. 4(a)).

3.3. Interaction model of dislocation and ODS

The dispersion of oxide particles in ODS HEAs impedes the movement of dislocations, thereby significantly influencing the mechanical properties of alloys [51–53]. Oxide particles are generally considered to be strong obstacles that cannot be cut by dislocations. When the dislocation is close to the oxide particle on the slip plane, the dislocation will bend and bypass the oxide particle, eventually leaving an Orowan loop around it [32–34]. With the advancement of experimental techniques and the extensive investigation of oxide particles, it has been observed that the large-sized oxide particles exhibit an incoherent state with the matrix, whereas the small-sized oxide particles demonstrate a coherent or semi-coherent state [35–38]. The relevant experimental findings provide favorable evidence that dislocations can cut the nanoscale oxide particle. Consequently, numerous recent studies have suggested that the nanoscale oxide particles can be cut by dislocations [54]. Therefore, a new oxide particle strengthening model, in which oxide particles can be cut by dislocations at small sizes, is established and embedded into the original DDD code to simulate the experimentally observed interactions between the oxide particles and dislocations.

Outside the nanoscale oxide particles, a Gaussian potential field is utilized to describe the short-range interaction of dislocations and the continuous force field caused by oxide particles, similar to the traditional oxide dispersion strengthening model in DDD simulations [55–58]. Therefore, large-sized oxide particles cannot be cut by dislocations due to the presence of high-stress fields around them. For small oxide particles, dislocations overcome the limited stress field surrounding the particles and cut the oxide particles. Since small oxide particles are coherent with the matrix, both coherent strengthening and modulus mismatch have limited impact. Therefore, the order strengthening dominates the interaction process of dislocation cutting through the small-sized oxide particles [59,60]. Thus, the interaction force between dislocations and oxide particles is written as

$$F(r) = \begin{cases} 2Are^{-\frac{r^2}{R^2}}/R^2 & r > R \\ -\gamma/b & r < R \end{cases} \tag{13}$$

where r is the distance between the center of the oxide particle and the dislocation node, R is the radius of the oxide particle, γ is the antiphase boundary energies of the oxide particle, b is the magnitude of Burgers vector, A is a constant quantifying the pinning strength of the oxide particle. A schematic of the interaction force between the dislocation and the oxide particle is presented in Fig. 5(a). With the slip dislocation close to the oxide particles, the force of the oxide particles exerting on dislocation nodes increases gradually. The interaction force reaches the maximum when the dislocation enters the oxide particle. Based on this interaction model, the cutting mechanism of the small-sized oxide particles and the Orowan mechanism in large-sized oxide particles are well simulated in DDD (Fig. 5(b)).

The irradiation hardening behavior of ODS FeCoCrNi HEA is extensively investigated by the collective behavior of dislocation using DDD simulation. The DDD simulation is based on ParaDiS, an open-source code developed by Lawrence Livermore National Laboratory. Severe lattice distortion, as the core effect of HEA, has an important effect on dislocation motion [61]. Therefore, it is necessary to develop DDD simulation considering severe lattice distortion field to study the interaction among dislocations, nanoscale oxides, and irradiation defects. Due to the limitation of the classical Eshelby mean field theory in DDD simulations, random field theory is used to quantify the strain field of FeCoCrNi HEA obtained by experiments [44]. Then, a fractal function of the experimental strain field is embedded into the original DDD code. Combined with the embedded lattice strain field, a series of DDD simulations is conducted to study the irradiation hardening of ODS FeCoCrNi HEA at mesoscopic scale.

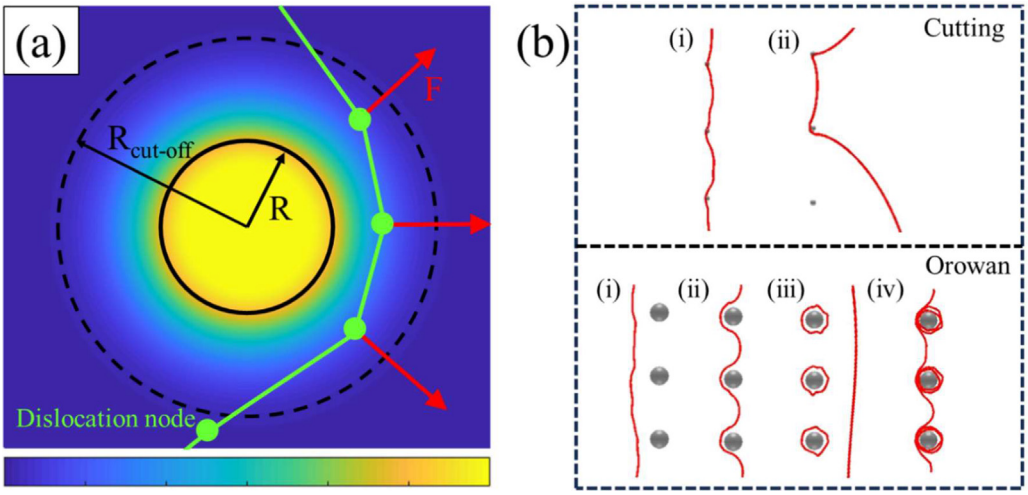

Fig. 5. (a) The schematic diagram of the interaction between oxide particle and dislocation. (b) The interaction between the dislocation and oxide particles with different sizes in DDD simulation. The colors represent the magnitude of the forces caused by the oxide particle exerted on the dislocation node at various locations in (a).

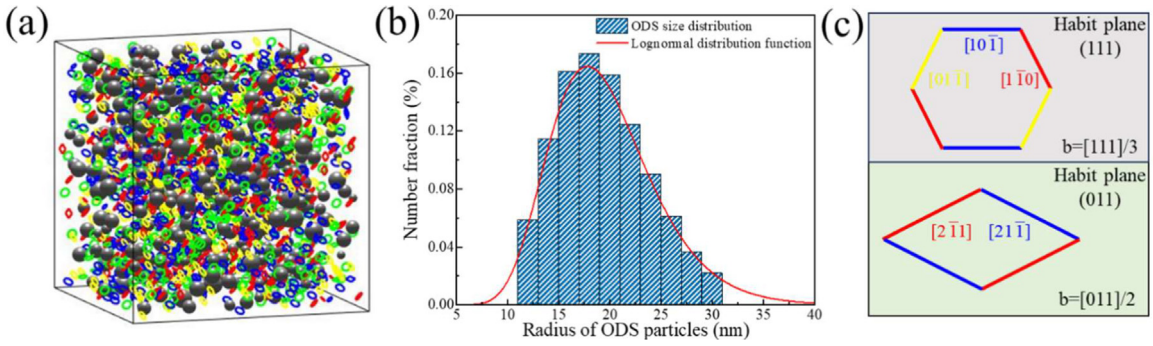

Fig. 6. (a) A schematic of the initial model of the DDD simulation. (b) The size distribution of a lognormal distribution of nanoscale oxides for DDD simulation. (c) Diagram of two dislocation loop configurations. The color indicates the different directions of the dislocations.

The simulation box is a cube with a size of 0.75 μm × 0.75 μm × 0.75 μm, and periodic boundary conditions are considered on all surfaces to simulate the bulk properties of the crystal. A constant strain rate of 1×10^6 s^{-1} is applied along the direction of [001] [56]. The schematic diagram of the established initial DDD model is shown in Fig. 6(a). The initial DDD model is established based on the number and characteristics of the experimental observed nanoscale oxides and irradiation defects in ODS FeCoCrNi HEA [62,63]. Ten initial dislocation lines are randomly distributed on the {111} ⟨110⟩ slip plane, corresponding to an initial density of $2.5 \times 10^{13} m^{-2}$. The mean particle radius of nanoscale oxide is 19 nm and the number density is 2.3×10^{21} m^{-2} [63]. For the actual size of nanoscale oxide in ODS HEA is not a single size, a lognormal distribution of nano-oxide size is considered, as shown in Fig. 6(b). According to recent experimental studies, the main defect leading to irradiation hardening of FeCoCrNi HEA is dislocation loops [64]. Two types of dislocation loops are observed experimentally in irradiated FeCoCrNi HEA, including elliptical Frank loops with $\boldsymbol{b} = 1/3 < 111 >$ and rhombus perfect loops with $\boldsymbol{b} = 1/2 < 110 >$ (Fig. 6(c)). The major axis of the elliptical Frank loops is along the ⟨110⟩ directions. The ratio of elliptical Frank loops to rhombus perfect loops is about 3:1 [64]. The aspect ratio of elliptical Frank loops is about 1. Hence, it is considered to have the shape of a hexagon in the DDD model. All six edges of the Frank loop are distributed on the {111} habit plane along the direction of ⟨110⟩. The rhombus perfect loops are located on the {110} habit plane, with two adjacent edges along the [211] and [$\bar{2}$11] directions, respectively [64,65]. Fig. 6(c) shows the structure of a Frank dislocation loop and a perfect dislocation loop. The radius and density of the dislocation loop vary with irradiation of the dose, as shown in Table 2. Some material parameters associated with the DDD simulation are listed in Table 3.

3.4. Damage model

Currently, the criteria for predicting material failure mainly include three categories, namely, the energy criteria, the equivalent stress-strain criteria, and the critical plane criteria. Among them, Von Mises criterion and Tresca criterion are the two most representative methods [66]. For the ODS FeCoCrNi HEA, the yield failure is the main mode.

Based on the theory of the distortion energy density, the Von Mises stress is generally used as the index for the prediction of failure, the value is calculated by the stress component:

$$\sigma_{ef} = \sqrt{\frac{1}{2}[(\sigma_x - \sigma_y)^2 + (\sigma_y - \sigma_z)^2 + (\sigma_z - \sigma_x)^2 + 6(\sigma_{xy}^2 + \sigma_{yz}^2 + \sigma_{zx}^2)]} \tag{14}$$

Therefore, assuming that the external force field is a uniform field, the stress field evolution of the DDD simulation process mainly includes two parts: the stress field of dislocation and oxide particles.

$$\sigma = \sigma_{dis} + \sigma_{ODS} \tag{15}$$

Table 2
The variation of radiation defect at different damage levels of the radiated FeCoCrNi HEA [64].

Parameter	Value			
Damage level (dpa)	0.036	0.102	0.170	0.326
Mean radius (nm)	5.175	9.716	14.555	22.134
Density (10^{21} m^{-3})	5.500	5.812	6.170	6.236

Table 3
The material parameters of the ODS FeCoCrNi HEA [63].

Parameter	Symbol	Value
Shear modulus	G	80 GPa
Poisson's ratio	ν	0.28
Burgers vector	b	0.254 nm
Dislocation core radius	r_0	0.254 nm

where σ_{dis} is the stress field caused by dislocation and σ_{ODS} is the stress field caused by dispersed oxide particles in the matrix.

Refer to the previous works about damage stress, a damage index D is introduced, and the value is determined by the ratio of the real stress to the yield stress [67,68]:

$$D = \frac{\sigma_i - \sigma_u}{\sigma_u} \tag{16}$$

where σ_i is the local stress of the ODS HEA, and σ_u is the allowable stress. In the region with $D > 0$, the material is considered as the damaged state. Here, σ_u is equal to the yield strength.

An expression for the three-dimensional dislocation configuration of the dislocation stress field is employed [69,70]. The stress field of a finite length dislocation segment with the endpoints x_1 and x_2 is given in a three-dimensional space:

$$\sigma_{ij}^{ns}(\boldsymbol{x}) = \frac{\mu}{8\pi}\int_{\boldsymbol{x_1}}^{\boldsymbol{x_2}} \partial_l\partial_p\partial_p R_a b_k\left(\varepsilon_{ilk}\mathrm{d}x'_j + \varepsilon_{jlk}\mathrm{d}x'_i\right) + \frac{\mu}{4\pi(1-\nu)}\int_{\boldsymbol{x_1}}^{\boldsymbol{x_2}} b_k\varepsilon_{lkm}\left(\partial_l\partial_i\partial_j R_a - \delta_{ij}\partial_l\partial_p\partial_p R_a\right)\mathrm{d}x'_m \tag{17}$$

where $\boldsymbol{x}$ is the field point, and x' is the source point. ∂_i, ∂_j, ∂_l, ∂_p represents differential, $\partial_i \equiv \partial/\partial x_i$, ε is the Levi-Civita symbol, b_k is the component of the Burgers vector of the dislocation, $R_a = \sqrt{(x_k - x'_k)^2 + r_0^2}$ and r_0 is the width of dislocation core.

The result of the integration is calculated as

$$\sigma^{\mathrm{dis}}(x) = T(R_2) - T(R_1) \tag{18}$$

and

$$T(\boldsymbol{R}) = T_0\Big\{[(\boldsymbol{R}\times\boldsymbol{b})\times\boldsymbol{t}][a_1(\boldsymbol{R}\otimes\boldsymbol{R}) + a_2(\boldsymbol{R}\otimes\boldsymbol{t}+\boldsymbol{t}\otimes\boldsymbol{R}) + a_3(\boldsymbol{t}\otimes\boldsymbol{t}) + a_4\boldsymbol{I}] + a_5[(\boldsymbol{R}\times\boldsymbol{b})\otimes\boldsymbol{t}+\boldsymbol{t}\otimes(\boldsymbol{R}\times\boldsymbol{b})] + a_6[(\boldsymbol{t}\times\boldsymbol{b})\otimes\boldsymbol{R}+\boldsymbol{R}\otimes(\boldsymbol{t}\times\boldsymbol{b})] + a_7[(\boldsymbol{t}\times\boldsymbol{b})\otimes\boldsymbol{t}+\boldsymbol{t}\otimes(\boldsymbol{t}\times\boldsymbol{b})]\Big\} \tag{19}$$

where $R_1 = x - x_1$, $R_2 = x - x_2$, and $\boldsymbol{t} = \frac{x_2 - x_1}{\|x_2 - x_1\|}$. T_0 is a constant related to the material, and $T_0 = \frac{\mu}{4\pi(1-\nu)}$. μ and ν are the shear modulus and Poisson's ratio. $\boldsymbol{I}$ is the identity matrix. a_1, a_2,....., a_7 are constants associated with the location of the spatial coordinates. The expressions are $a_1 = \frac{\boldsymbol{R}\cdot\boldsymbol{t}[(\boldsymbol{R}\cdot\boldsymbol{t})^2 - 3R_0^2]}{(R_0^2 - (\boldsymbol{R}\cdot\boldsymbol{t})^2)^2 R_0^3}$, $a_2 = \frac{1}{R_0^3} - a_1(\boldsymbol{R}\cdot\boldsymbol{t})$, $a_3 = -\frac{\boldsymbol{R}\cdot\boldsymbol{t}}{R_0^3} - \frac{\boldsymbol{R}\cdot\boldsymbol{t}}{(R_0^3 - (\boldsymbol{R}\cdot\boldsymbol{t})^2)^2 R_0} + a_1(\boldsymbol{R}\cdot\boldsymbol{t})^2$, $a_4 = -\frac{\boldsymbol{R}\cdot\boldsymbol{t}}{(R_0^2 - (\boldsymbol{R}\cdot\boldsymbol{t})^2)^2 R_0} + a_1 r_0^2$, $a_5 = a_1\frac{r_0^2(\nu-1)}{2} - \frac{\boldsymbol{R}\cdot\boldsymbol{t}}{(R_0^3 - (\boldsymbol{R}\cdot\boldsymbol{t})^2)^2 R_0}(\nu - 1)$, $a_6 = a_4 - a_1 r_0^2$, $a_7 = \frac{\nu}{r_0} - a_6(\boldsymbol{R}\cdot\boldsymbol{t}) - a_2\frac{r_0^2(1-\nu)}{2}$, and $R_0 = \sqrt{\|R\|^2 + r_0^2}$.

Based on the equivalent inclusion method, the disturbance stress field caused by the inclusion is equivalent to the characteristic stress field caused by the eigenstrain. The oxide particles dispersed in ODS HEA are regarded as spherical inclusions. According to Mura and Eshelby's micromechanics theory, the stress field distribution of oxide particles on the matrix is written in the form of an auxiliary symmetric tensor [70]:

$$\boldsymbol{p} = 2\mu(\varepsilon^* + \frac{\nu}{1-2\nu}tr(\varepsilon^*)\boldsymbol{I}) \tag{20}$$

where ε^* is a transformation-strain tensor and $\varepsilon^* = \delta\boldsymbol{I}$. $\boldsymbol{I}$ is the identity matrix. δ is the lattice misfit between the oxide particles and matrix, and calculated as $\delta = \frac{d_p - d_M}{d_M}$, where d_p is the atomic plane distances of oxide particle, and d_M is the interplanar spacing of the matrix.

The stress field inside the oxide particles is [70]:

$$\boldsymbol{\sigma}_{in} = 2\mu[(L + \frac{(3L+2M)}{1-2\nu}\nu)tr(\varepsilon^*)\boldsymbol{I} + 2M\varepsilon^*] - \boldsymbol{p} \tag{21}$$

where L and M are constants related to the material, and $L = \frac{5\nu-1}{15(1-\nu)}$, $M = \frac{4-5\nu}{15(1-\nu)}$. ν is the Poisson's ratio.

According to the thermal expansion theory, the stress field outside the oxide particle is [58,70–72]

$$\boldsymbol{\sigma}_{out} = \boldsymbol{\sigma}_{in}(r_0/R)^3 \tag{22}$$

4. Results

4.1. Validity of DDD simulation

Based on the established model, a series of samples with different oxide particle densities and irradiation doses are simulated by DDD. The radius of the oxide particle is 19 nm according to the previous experiments [62,63]. The stress–strain curves for the samples with different oxide particle densities are presented in supplemental material (Fig. S1 in the Supplementary Material).

The Bacon–Kocks–Scattergood (BKS) model is a widely accepted dislocation-obstacle hardening model, which establishes the relationship between yield strength and obstacle through the dislocation line tension approximation [56,73]. The stress caused by the oxide particle in the BKS model is expressed as:

$$\sigma_{ODS} = A\frac{Gb}{L - D_p}\left(\ln\left(\overline{D}_p/b\right) + B\right) \tag{23}$$

where $A = 1/(2\pi)$ is a constant associated with the characteristics of the dislocation, G is the shear modulus, and b is the Burgers vector. $L = (2D_p\rho_p)^{-0.5}$ is the distance between the nanoscale oxides in the glide plane, where D_p and ρ_p are the diameter and number density of oxide particles, respectively. $\overline{D}_p = (D_p^{-1} + L^{-1})^{-1}$ is the harmonic average of L and D_p. $B = 0.7$ is a constant [56,73]. The DDD simulation results from the established model are compared with the classical BKS model in Fig. 7(a). The simulation results are in good agreement with the BKS model, indicating that the established DDD model can accurately reproduce the dispersion-strengthening effect of oxide particles.

In Fig. 7(b), the stress–strain curves of samples with different radiation doses are obtained using DDD simulation. The results are compared with a well-established dispersed barrier-hardening (DBH) model to verify whether the established model can accurately capture the effect of irradiation-induced dislocation loops.

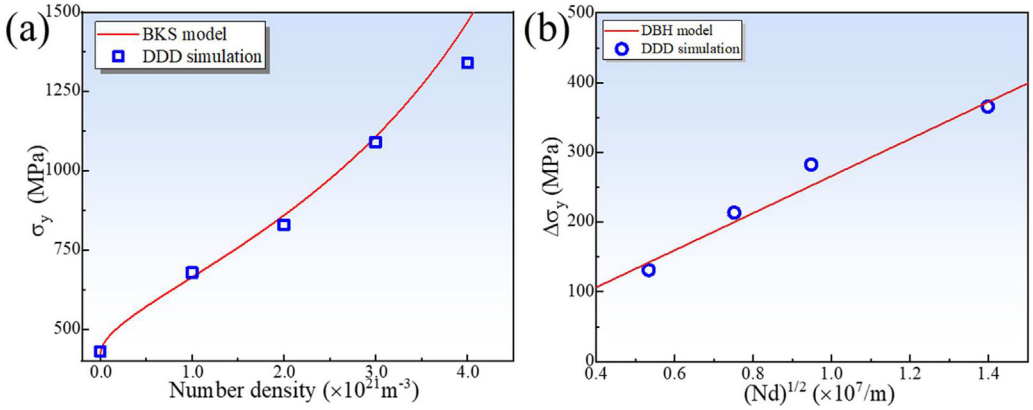

Fig. 7. (a) The correlation between the yield strength and the number density of oxide particles. (b) The correlation between the strengthening increment from irradiation defect and the square root of the product of defect density and size.

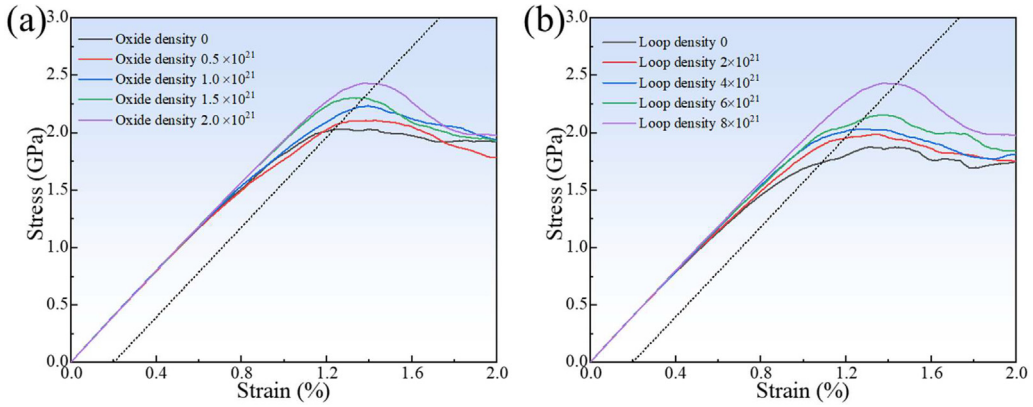

Fig. 8. (a) The stress–strain curves of the ODS HEA for different nanoscale oxide densities and a dislocation loop density of 8×10^{21} m^{-3}. (b) The stress–strain curves of ODS HEA for different dislocation loop densities and a nanoscale oxide density of 2×10^{21} m^{-3}.

According to the DBH model, the yield strength increment from oxide particles is expressed as [63,74]:

$$\Delta\sigma_y = \alpha MGb(ND_b)^{1/2} \quad (24)$$

where M is the Taylor factor, which is 3.06 for the FCC structured HEA. α is a constant for the average barrier strength, $\alpha = 0.4$ is accepted for strong obstacles such as dislocation loops [74]. G is the shear modulus, b is the Burgers vector, D_b is the dislocation loop diameter, and N is the number density of the dislocation loop. As shown in Fig. 7(d), the results of the DDD simulation show a good linear correlation with the DBH model, which demonstrates the DDD simulation captures the irradiation hardening behaviors caused by the dislocation loops [74]. Therefore, the established DDD model accurately describes the interaction process between the dislocation and oxide particle (or dislocation loop). Thus, it is used to study the dislocation structure evolution under the coexistence of lattice distortion, oxide particle, and irradiation-induced dislocation loop. In addition, it may reveal the microscopic mechanism to influence the mechanical properties.

4.2. Dislocation evolution

In order to investigate the mechanical behavior and microstructural evolution of irradiated ODS HEA under loading conditions, a series of DDD simulations involving different oxide-particle and dislocation-loop densities is performed. The effect of the lattice distortion field is considered by embedding fractal strain field, consistent with the experiment. Two independent sets of samples are set by varying the oxide-particle and dislocation loop density, respectively. Fig. 8 shows the stress–strain curves. The yield strength of ODS HEA increases with the increase of oxide particle density due to the oxide particle impeding dislocation movement (Fig. 8(a)). The irradiation hardening caused by the dislocation loop is observed in Fig. 8(b). For all samples containing the irradiation-induced dislocation loops, the stress drop is observed after the yield, especially in the samples with high density of dislocation loop and oxide particle, which is consistent with Refs. [65,75]. The significant stress drop is attributed to the annihilation of the dislocation loops on the slip plane, and then leads to the formation of plastic flow localization and a defect-free channel [75–77]. For the sample with the oxide particle density of 2.0×10^{21} m^{-3} and dislocation loop density of 8.0×10^{21} m^{-3}, the stress–strain curve shows a large stress drop after yielding, attributed to the fact that the existence of lattice strain field makes a high probability of dislocation cross-slip. This trend results in the change of the dislocation slip plane, and a large number of dislocations slip to the plane with fewer oxide particles [44,78].

To investigate the microstructure dynamic evolution in the irradiated ODS HEA during the tensile deformation, Fig. 9 provides the dislocation structure snapshots at the increasing strains for varying densities of dislocation loops and oxide particles. The random distribution of dislocation loops and oxide particles is observed, and a small amount of dislocation multiplication occurs at the initial stage of deformation (Fig. 9). With the increase of plastic deformation, the area swept by the slip dislocation increases, and a large number of dislocation loops are annihilated during the dislocation interaction [79]. The annihilation of dislocation loops near the slip plane leads to the formation of defect-free channels, which is accompanied by a large

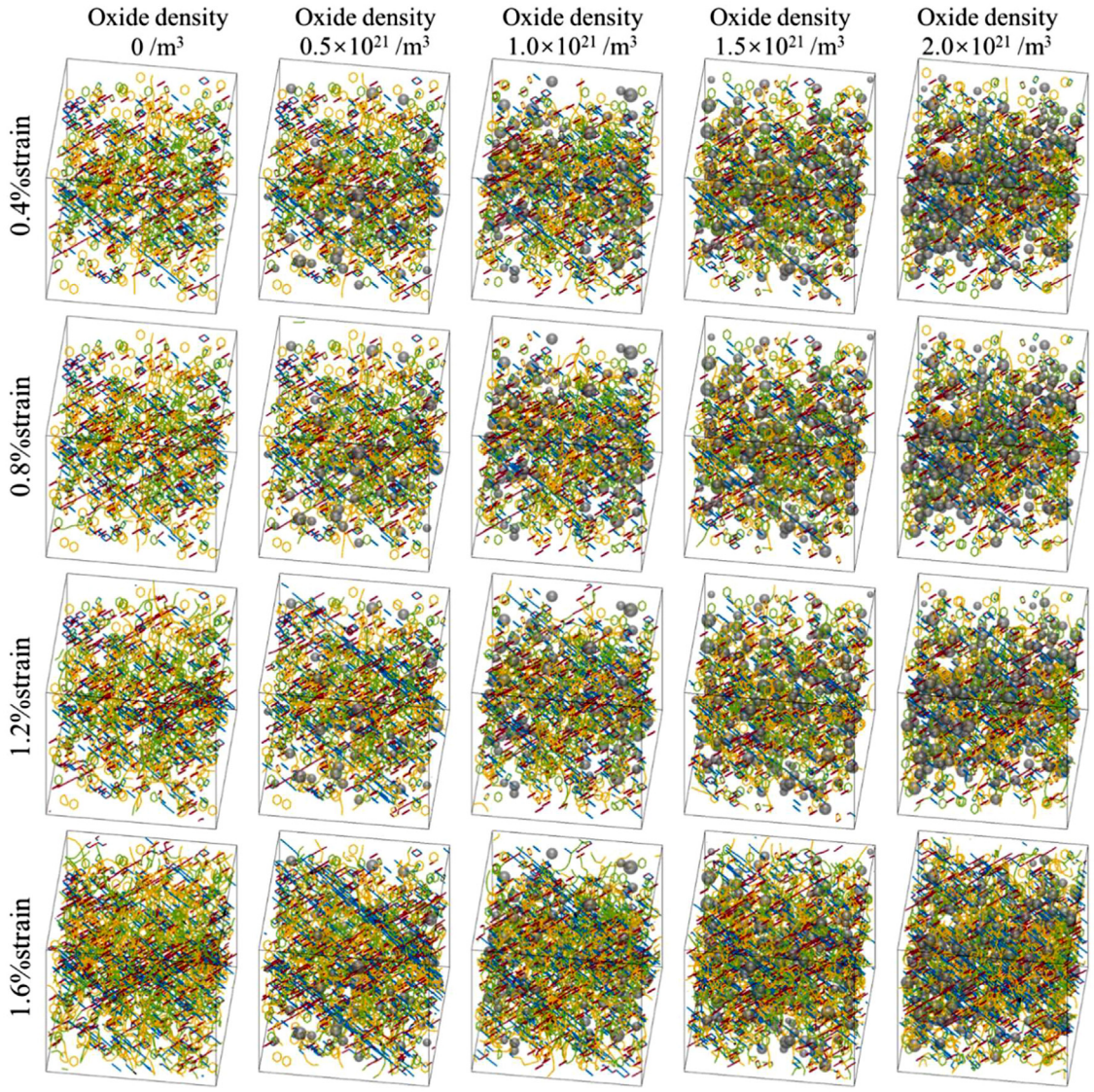

Fig. 9. Dislocation structure at the strains of 0.4%, 0.8%, 1.2%, and 1.4% for different oxide particle densities in ODS HEA. The dislocations on the (111) slip plane are marked with blue line (——), ($\bar{1}11$) slip plane with red line (——), ($1\bar{1}1$) slip plane with yellow line (——), ($11\bar{1}$) slip plane with green line (——), and other slip planes with blank line (——).

number of dislocation multiplication [21,80]. With the appearance and increasing density of oxide particles, there is no significant change in the number of dislocations observed during the initial elastic stage. However, a large number of dislocation multiplications are observed during the plastic deformation stage. In addition, Orowan loops are observed around some large-size oxide particles.

Fig. 10 shows the dislocation structure evolution during the material deformation at various dislocation loop densities with the oxide particle density of 2.0×10^{21} m^{-3}. Due to the impediment of the high-density oxide particles, only a small amount of dislocation slip occurs in the initial deformation, and the deformation mode is mainly elastic deformation. With the increase of dislocation loop density, the frequency of interactions between dislocation and dislocation loops increases with the continuous deformation. As the stress increases, the dislocations either bypass the large-size oxide particles or cut the small-size oxide particles. The interaction between dislocations and dislocation loops leads to not only the annihilation of dislocation loops but also the formation of a few jogs [78,79].

Fig. 11 shows the variation of the dislocation density with the strain. The movable and immovable dislocation density is based on the statistics of dislocation segments and the Schmid factor. For an FCC crystal with the loading direction [001], the Schmid factor of dislocations with Burgers vectors of [110]/2 and [$\bar{1}$10]/2 is zero. Thus the corresponding slip system is not activated. Therefore, the statistical immobile dislocations include the Burgers vector of [110]/2, [$\bar{1}$10]/2 and others that do not belong to the 12 slip systems of FCC crystal. For the sample with oxide particles in the matrix, the immobile dislocation density increases with the increase of oxide particle density (Figs. 9 and 11(a)). The more oxide particles on the slip plane hinder the movement of the dislocation, and some dislocations bypass the oxide particles and leave Orowan loops, resulting in a large number of immobile dislocations (Fig. 9). Interestingly, the samples without oxide particles do not exhibit the low dislocation density, attributed to that the material yields early, and a large amount of dislocation proliferation occurs in the plastic stage. In addition, the densities of the immobile and mobile dislocations go up with the increase of dislocation loop density, as shown in Figs. 10 and 11(b). The existence of

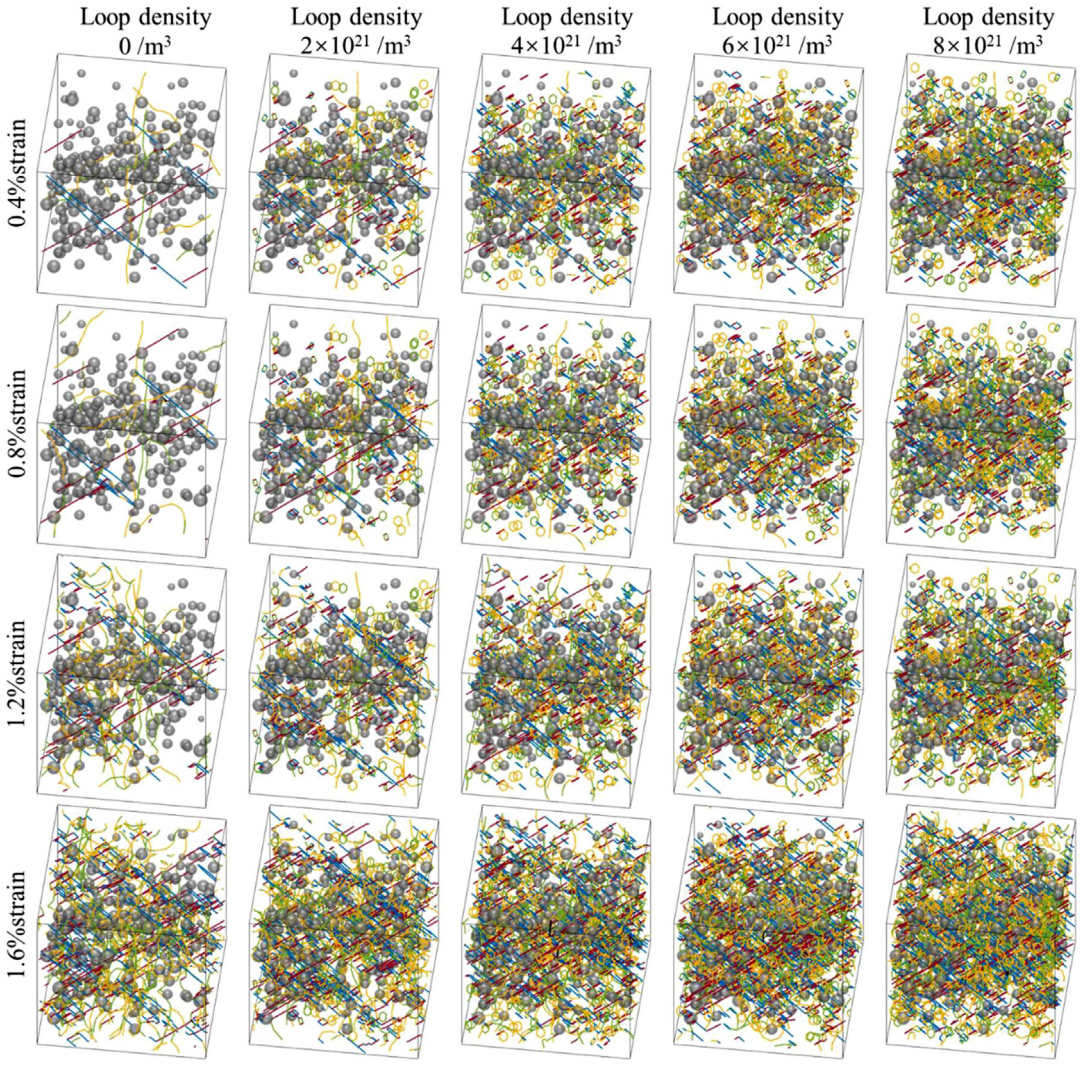

Fig. 10. Dislocation structure at the strains of 0.4%, 0.8%, 1.2%, and 1.4% for different dislocation loop densities in ODS HEA. The dislocations on the (111) slip plane are marked with blue line (——), ($\bar{1}11$) slip plane with red line (——), ($1\bar{1}1$) slip plane with yellow line (——), ($11\bar{1}$) slip plane with green line (——), and other slip planes with blank line (——).

the dislocation loops frequently interacts with the dislocation, and then promotes the production of cross-slips and jogs [81–83]. The dislocation-based microstructures are hard to annihilate, and cause a high density of dislocations, which is consistent with the observations from Figs. 9 and 10.

5. Discussion

5.1. Damage evolution

Fig. 12 shows the dislocation structure, Von Mises stress field, and damage distribution at the irradiated ODS HEA before loading. It should be noted that the oxide particles do not cause stress damage, attributed to the isotropic characteristics of the stress field according to the classical inclusion theory [84]. Here, the irradiation-induced dislocation loops randomly distribute in the matrix, resulting in a high local stress field and initial dislocation loop damage in the ODS HEA (Fig. 12(a)). The initial damage is characterized by the loop shape, indicating that the local high-stress field and damage are caused by the high density of irradiation-induced dislocation loops (Fig. 12(b, c)).

To highlight the submicron scale continuous damage, Fig. 13(a–c) shows the evolution of the dislocation structure, Von Mises stress field, and stress damage. As the ODS HEA is loaded from the strain of 0% to 0.3%, a small amount of dislocation slip occurs at the elastic stage, some dislocation loops are annihilated from the interaction with the slip dislocation, and a small number of Orowan loops are produced around the larger oxide particles (Fig. 13(a)). At the stage of 0.6% strain, a large amount of irradiation-induced dislocation loops are annihilated, and a small number of Orowan loops are generated. The damage caused by the irradiated dislocation loops decreases, and the damage caused by dislocation entanglement and Orowan loops gradually increases [85,86], as shown in Fig. 13(c). At the strain of 0.9% and 1.2%, a large amount of dislocation multiplication occurs, and thus the local plastic deformation of the material increases significantly. Due to the oxide particles impeding the formation of Orowan loops and the dislocation movement, a large number of dislocations pile up around oxide particles, resulting in high local stress (Fig. 13(b)). Therefore, with the increase of strain, the damage gradually changes from the random distribution to the concentrated distribution around the oxide particles (Fig. 13(c)). In order to investigate the damage degree during the deformation process, Fig. 13(d) calculates the probability of damage grade at each strain level. The statistical results suggest that the damage probability reduces at the strain increasing from 0% to 0.6%, ascribed

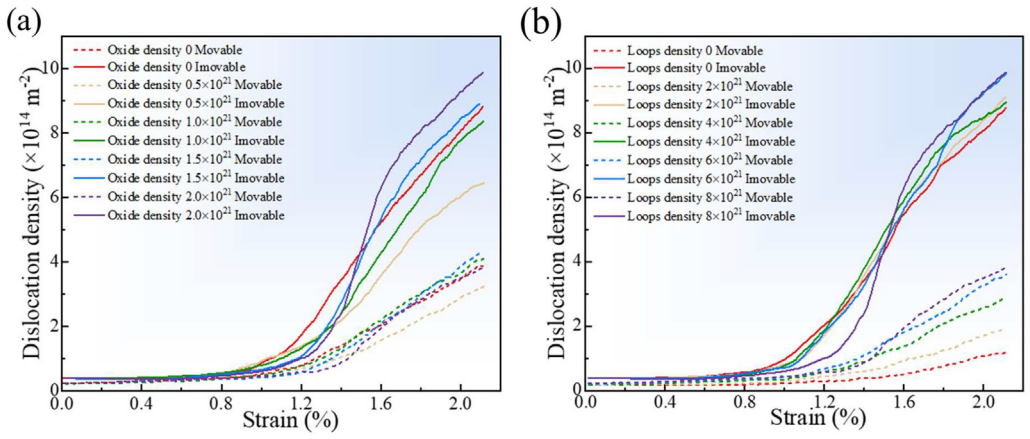

Fig. 11. The statistical density of movable and immovable dislocations. (a) Effect of oxide particle density and (b) dislocation loop density.

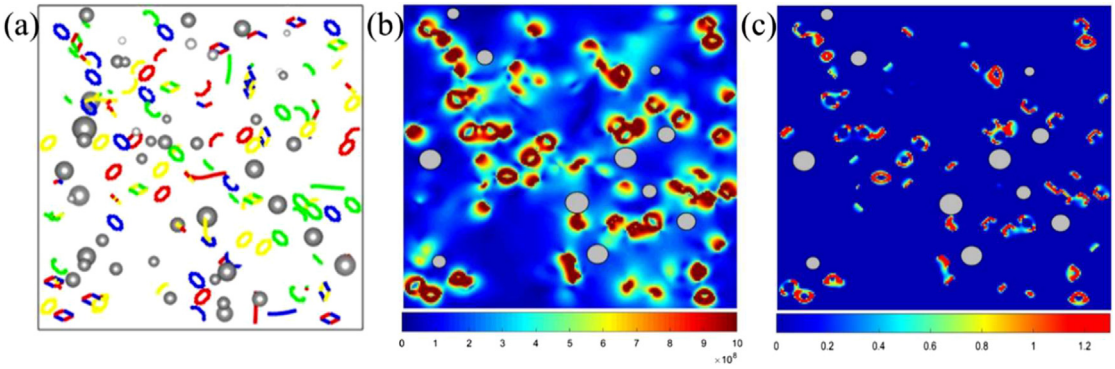

Fig. 12. (a) The initial dislocation configuration, (b) Von Mises stress, and (c) damage distribution in the sample with oxide particle density of 2 × 10^{21} m^{-3} and dislocation loop density of 6 × 10^{21} m^{-3}.

to the annihilation of part of the dislocation loops [21]. For the strain increasing from 0.6% to 1.2%, the dislocation loops on the slip plane are almost annihilated, and the reduction rate of the damage caused by the dislocation loop is reduced [87]. Besides, the dislocation motion resistance is greatly reduced because of the formation of the defect-free channels, and then leads to the dislocation multiplication, tangles, and Orowan loops. Therefore, there is a large amount of dislocation pile-up to cause serious damage in the local area, especially around the oxide particles.

Based on the above-mentioned damage evolution, the damage mechanism in the ODS HEA is divided into two parts: (i) the dislocation loop damage (D_l) controlled by irradiation-induced dislocation loops and their evolution, and (ii) the strain localization damage (D_s) from the dislocation multiplication in the local plastic region. Fig. 14 presents the strain localization damage and dislocation loop damage with the increasing strain, which would reveal the mechanism of the counterintuitive decreasing-to-increasing damage transition. In the statistics of the two damage modes, the stress fields from the dislocation loop and slipping dislocation are separately considered. Fig. 14 clearly captures the gradual decrease of the dislocation loop damage and the continuous increase of the strain localization damage, which are caused by dislocation loop annihilation and dislocation multiplication. The dislocation loop damage is the main mechanism in the elastic damage stage, and the strain localization damage plays a dominant role in the plastic damage stage. At a low strain, the reduction rate of dislocation loop damage exceeds the increase rate of strain localization damage; at high strain, it is opposite, resulting in the decreasing-to-increasing damage transition.

To accurately display the relationship between damage distribution and microstructures, Fig. 15 shows the local enlarged drawings of the damage evolution in the ODS HEA. At the elastic stage, a large number of irradiated dislocation loops exist, and lead to a local high damage. The damage of the irradiated ODS HEA decreases slightly due to the annihilation of dislocation loops. However, the damage gradually increases with the continuous increase of strain. Here, no dislocation plugging around the smaller oxide particle is observed, due to that (i) the small-size oxide particle is not conducive to the formation of Orowan loops; (ii) the oxide particle is away from the dislocation slip plane.

5.2. Dislocation behavior

At the elastic damage stage in the irradiated ODS HEA, the annihilation for a large number of dislocation loops is observed, resulting in a reduction of dislocation loop damage. To study the influence of the dislocation loop and heterogeneous lattice strain on dislocation-induced damage, the interaction of dislocation loops with a single dislocation is investigated. The cases with and without lattice strain fields are considered separately. In addition, some dislocation loops do not react with the dislocations, they may maintain the original structure or they may be deformed under the effect of the stress (Fig. S2). Fig. 16 illustrates the interaction process of rhombus perfect dislocation loops with Burgers vector of $1/2[01\bar{1}]$ and habit plane of $(01\bar{1})$ and an edge dislocation with Burgers vector of $1/2[10\bar{1}]$ and slip plane of (111). When there is no lattice strain field, the shear stresses first increase and then decrease. After the ultimate stress is reached, there is a significant stress drop which indicates the rapid deterioration of properties (Fig. 16(a)). Fig. 16(b) shows the dislocation evolution diagram owing to some dislocation loops overcome by the dislocation, and the other dislocation loops are annihilated [65]. This type of disloca-

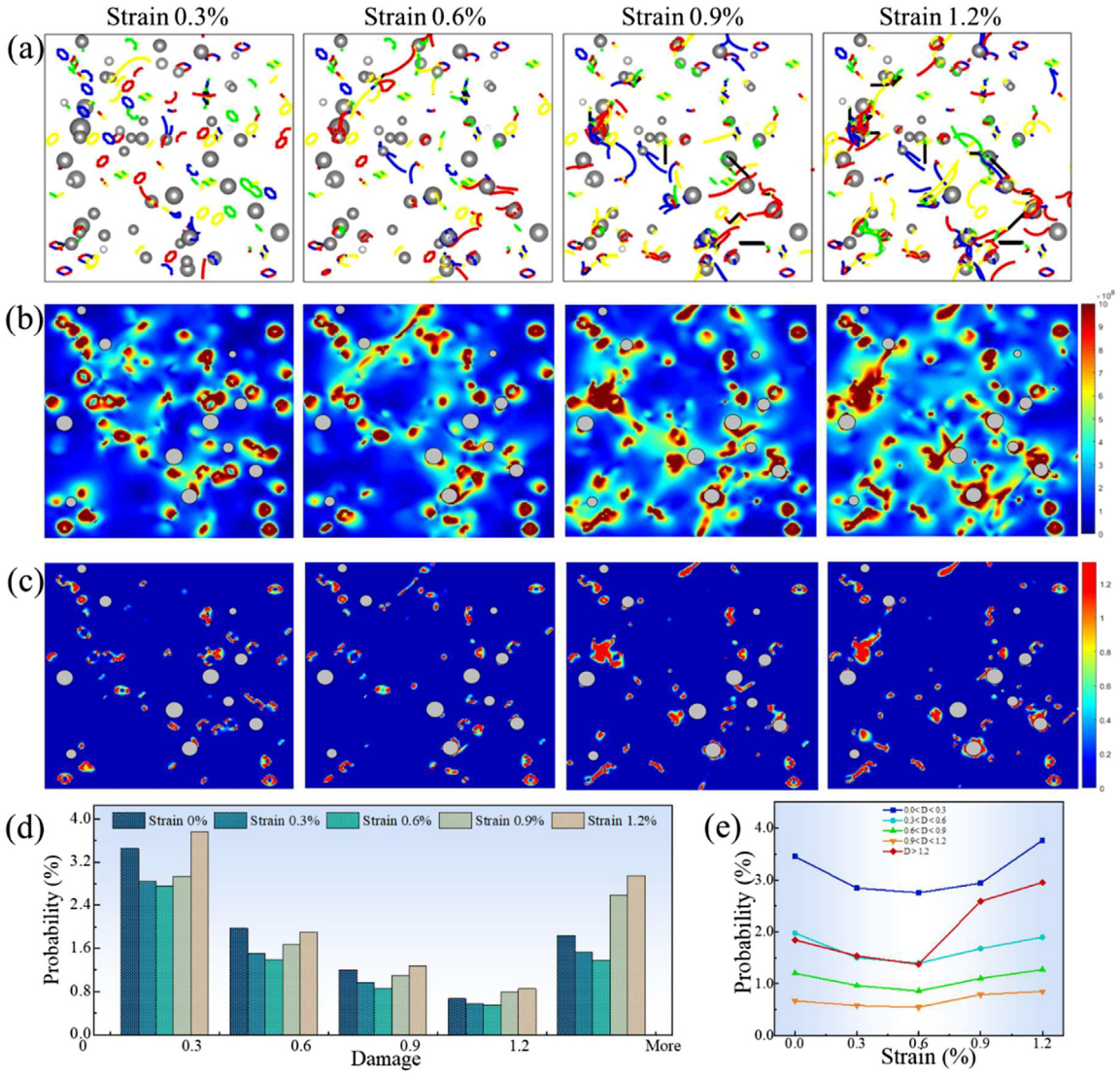

Fig. 13. (a) The dislocation configuration, (b) Von Mises stress, (c) damage distribution in the sample with the oxide particle density of 2.0×10^{21} m^{-3} and dislocation loop density of 6×10^{21} m^{-3} at the strain of 0.3%, 0.6%, 0.9% and 1.2%. (d) The statistics of damage distribution at different strains. (e) The proportion of different grades of damage as the function of strain.

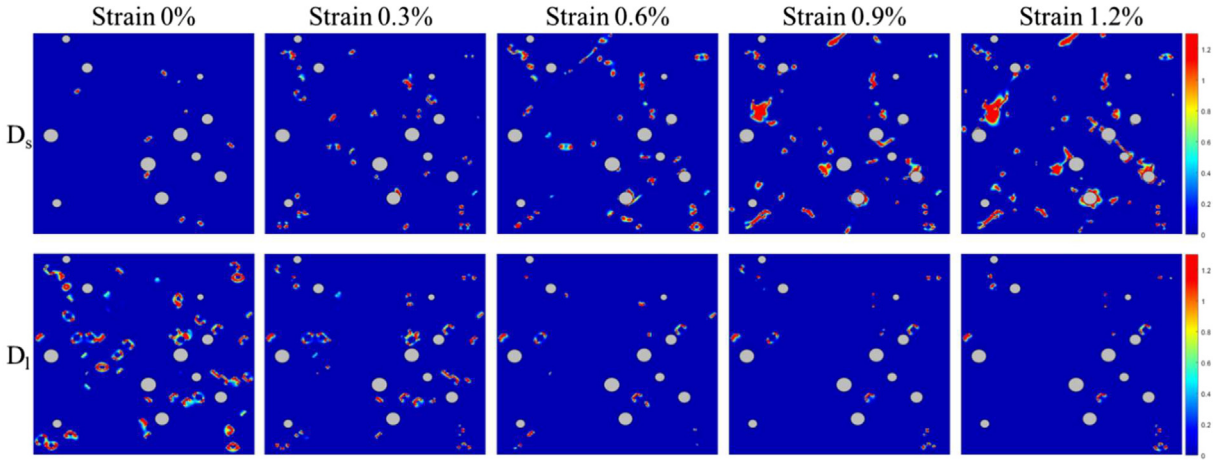

Fig. 14. The evolution of the strain localization damage (D_s) and dislocation loop damage (D_l) in the deformed ODS-HEA.

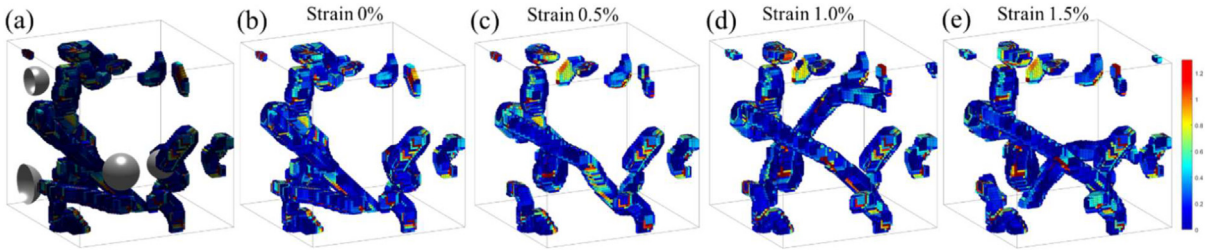

Fig. 15. The local enlarged drawing of the damage evolution with the increase of the strain in three-dimensional space. (a) Schematic diagram of the location of oxide particles. (b–e) The damage map of the ODS HEA at strains of 0%, 0.5%,1.0%, and 1.5%.

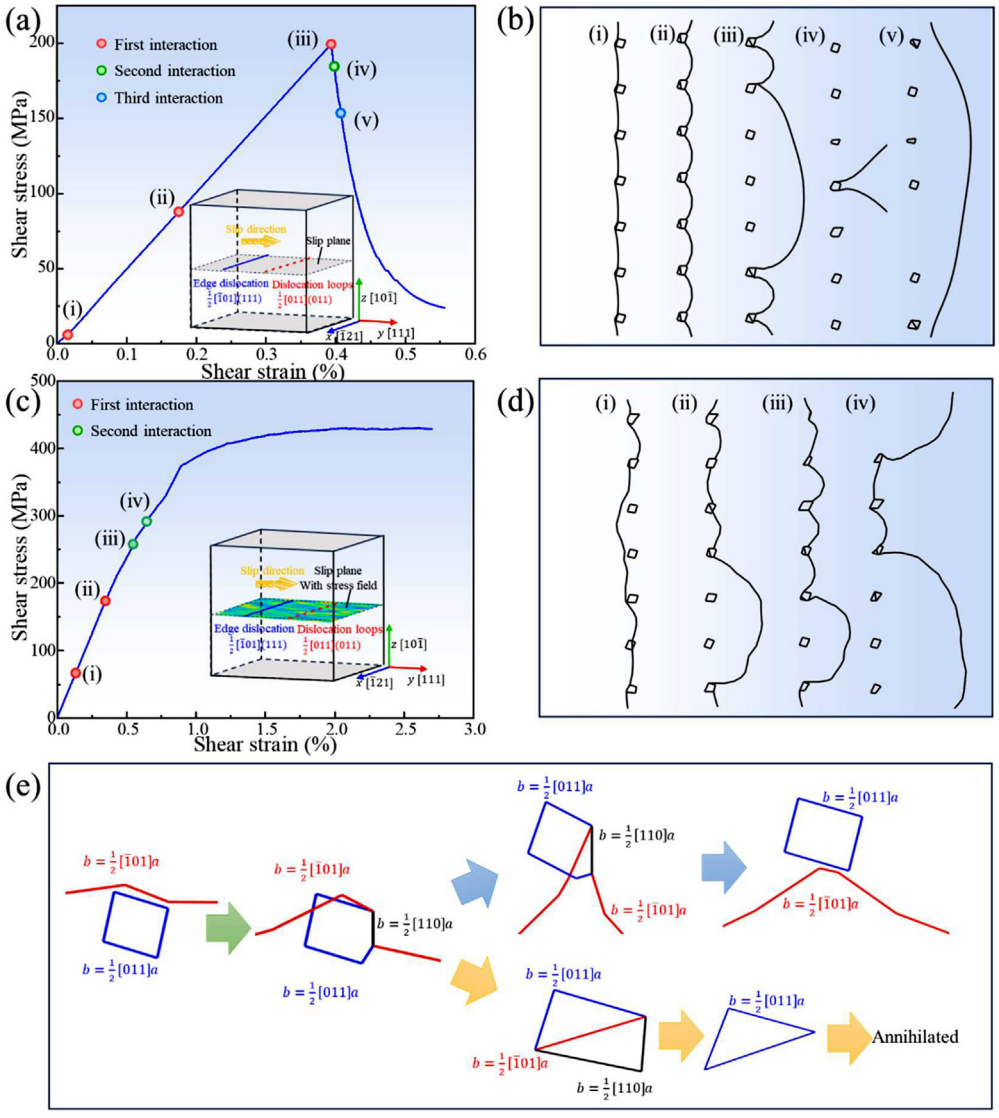

Fig. 16. (a) The shear stress–strain curves of the interaction between a dislocation and dislocation loop without local lattice distortion. (b) The corresponding snapshot of dislocation structure evolution. (c) The shear stress–strain curves of the interaction between a dislocation and dislocation loop with the local lattice distortion. (d) The corresponding snapshot of the dislocation structure evolution. Here, the dislocation has the Burgers vector of $1/2[10\bar{1}]$ on the slip plane of (111), and the rhomboid perfect loops have the Burgers vector of $1/2[01\bar{1}]$ on the habit plane of $(01\bar{1})$. (e) The magnified view of the interaction between an edge dislocation with Burgers vector of $1/2[\bar{1}01]$ slip plane of (111) and a rhomboid perfect dislocation loop with Burgers vector of 1/2[011] and habit plane of (011).

tion interaction contributes to the formation of defect-free channels. Considering the effect of the lattice strain field, Fig. 16(c) shows the shear stress–strain curve for the dislocation and dislocation loops interaction. With the influence of the strain field, the peak stress from the shear stress–strain curve of dislocation and Frank loops interaction increases obviously. There is no obvious stress drop after reaching the peak stress due to the strengthening effect of the lattice strain field [48,88]. It indicates that the lattice strain field effectively reduces the property degradation in the irradiated ODS HEA after a large number of dislocation loops are annihilated. In the diagram of the dislocation evolution (Fig. 16(d)), the bending of the slip dislocation suggests the slip resistance and

strengthening effect of the lattice strain field to prevent property deterioration. Interestingly, the dislocation loops exist after the initial reaction with the slip dislocation, but they are annihilated after multiple interactions observed in Fig. 16(b). The multiple interactions between the dislocation loops and dislocations result in the change of the collision distance between the dislocation, which promotes the occurrence of the dislocation reaction [89–91].

To deeply understand the complex dislocation interaction, two typical interactions between the dislocation and the perfect dislocation loop or the Frank dislocation loop are investigated. The detailed dislocation reaction process including the annihilated and non-annihilated process of perfect dislocation loops with the Burgers vector of 1/2[011] is shown in Fig. 16(e). When the edge dislocation with Burgers vector of $1/2[\bar{1}01]$ is close to the perfect dislocation loop with Burgers vector of 1/2[011], the dislocation reaction occurs:

$$\frac{1}{2}[10\bar{1}]a + \frac{1}{2}[011]a = \frac{1}{2}[110]a \tag{25}$$

When the perfect dislocation loops are not annihilated, the slip dislocation and the dislocation loops are separated after the reaction:

$$\frac{1}{2}[\bar{1}01]a + \frac{1}{2}[110]a = \frac{1}{2}[011]a \tag{26}$$

While the dislocation loops are annihilated, the dislocation structure is left after the separation of the slip dislocation and the dislocation loops (Fig. 16(e)). Then, one side of the dislocation loop firstly reacts with the dislocation in the middle, and the dislocation reaction agrees with Eq. (26). The triangular perfect dislocation loop left behind is annihilated, because the size is too small and the distance between the dislocations reaches the minimum distance for the dislocation reaction [92–94].

5.3. Effect of oxide particle on damage

Recent studies have demonstrated that HEAs have better irradiation hardening performance because of the more uniform distribution of defect-free channels caused by severe lattice distortion [21,94]. In order to further study the effect of oxide particles on the irradiation performance from the perspective of damage, Fig. 17 shows the snapshot of the dislocation structure, Von Mises stress field, damage distribution, and the corresponding statistical result. Fig. 17(a–c) reveals the samples without oxide particles have a high dislocation density. The statistics of the dislocation density show that the samples without oxide particles have almost the same density of immovable dislocations as the samples with oxide particles. However, samples without oxide particles have a high movable dislocation density (Fig. 17(c)), due to the existence of oxide particles to impede the dislocation movement and cause

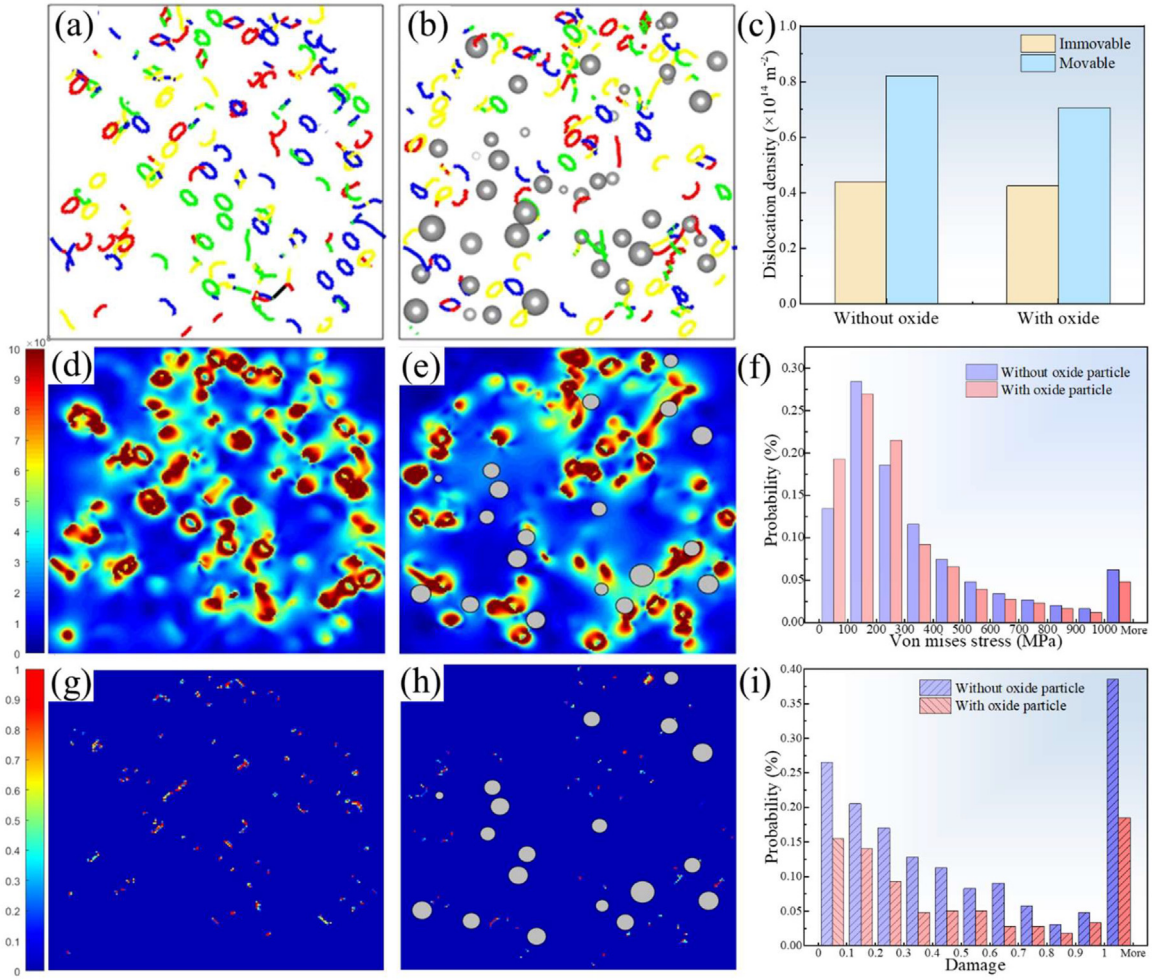

Fig. 17. Dislocation configuration for samples with dislocation loop density of 6×10^{21} m^{-3} at the strain of 1%: (a) without oxide particle, and (b) with oxide particle density of 2×10^{21} m^{-3}. (c) Density of movable and immovable dislocations in the samples with and without oxide particles. The irradiated dislocation loops are not included in the statistical dislocation density. The Von Mises stress fields: (d) without oxide particles and (e) with oxide particles. (f) The probability statistics of different stresses. The damage distribution of samples: (g) without oxide particles and (h) with oxide particles. (i) The probability statistics of damage.

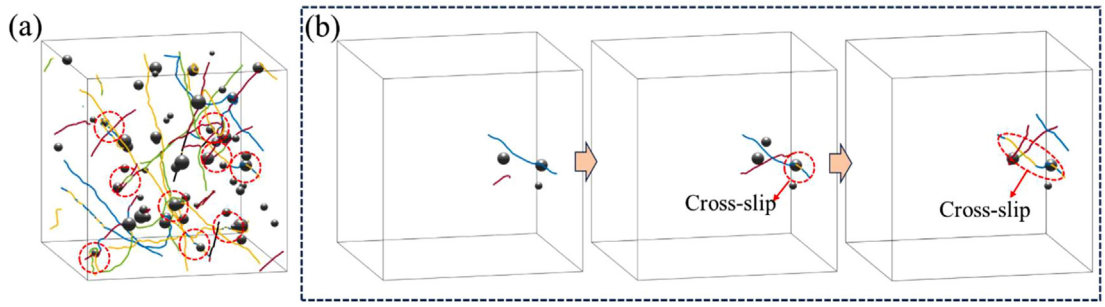

Fig. 18. (a) The dislocation structure diagram of the ODS HEA with the influence of lattice strain field. (b) The snapshots for the generation process of cross-slip. The dislocations on the (111) slip plane are marked with blue line (——), $(\bar{1}11)$ slip plane with red line (——), $(1\bar{1}1)$ slip plane with yellow line (——), $(11\bar{1})$ slip plane with green line (——), and other slip planes with blank line (——).

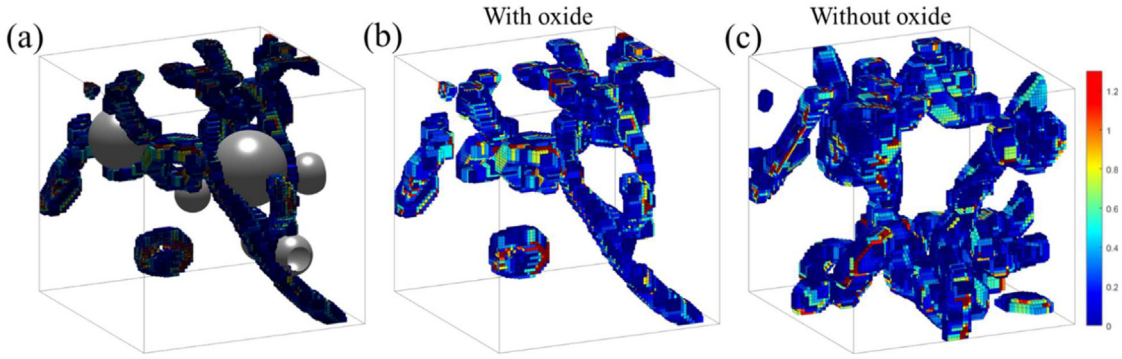

Fig. 19. (a) The location of oxide particles in local enlarged maps. The 3D local enlarged maps of damage distribution at a strain of 1%: (b) with oxide particle, (c) without oxide particle.

the reduction of dislocation multiplication [95,96]. Fig. 17(d, e) depicts the Mises stress fields. At the same strain, the Von Mises stress field and damage degree in ODS HEA is significantly lower than that in HEA (Fig. 17(d, e)), indicating the presence of oxide particles reduces the damage degree.

By observing the dislocation structure evolution near the oxide particles, a high cross-slip probability is found around the oxide particles. Fig. 18 shows the dislocation structure of the HEA. For the interaction with the oxide particles, a large number of cross-slips are observed at the slip dislocations, as marked in the red circle in Fig. 18(a). The local diagram shows the generation process of the cross-slip (Fig. 18(b)). The high frequency of cross-slip is attributed to the combined effect of oxide particle and lattice distortion field. The presence of oxide particles prevents the dislocation movement on the main slip plane, while the lattice strain field provides the driving force of the dislocation to the secondary slip plane. The frequent occurrence of cross-slips leads to plenty of interactions between the dislocation and dislocation loops. This trend results in the annihilation of the dislocation loops and the further generation of cross-slip. Irradiation damage decreases with the annihilation of dislocation loops [21]. In addition, it causes narrow and evenly distributed defect-free channels and low irradiation hardening.

On the one hand, the existence of oxide particles impedes the dislocation slipping, and prevents the dislocation multiplication, thus reducing the strain localization damage. On the other hand, it accelerates the annihilation of dislocation loops, and reduces the dislocation loop damage under the coupling effect of oxide particles and lattice distortion. Therefore, the damage degree of ODS HEA at the same strain is much lower than that of HEA (Fig. 17(g, h)). The damage statistical results show that the damage degree of ODS HEA is much smaller than that of HEA at the same strain (Fig. 17(i)). Hence, the hindering effect from oxide particles on dislocation motion and the synergistic effect from oxide particles and lattice distortions result in fewer dislocations and dislocation loops in irradiated ODS HEA. Therefore, ODS HEA has good service performance under irradiation conditions.

More importantly, Fig. 19 shows the 3D local enlarged maps of damage distribution in the ODS HEA. Under the same strain, the sample with oxide particles has a lower damage degree and smaller damage region than the sample without oxide particles (Fig. 19(b, c)). This is attributed to the presence of oxide particles hindering the movement of the dislocation, which prevents the plastic deformation process. Therefore, the strain localization damage of the sample with oxide particles is reduced. Due to large plastic deformation, dislocation multiplication, and dislocation loop annihilation, the strain localization damage is dominant. In addition, the local concentration of damage is notably observed near the large oxide particles. The large oxide particles have a strong ability to hinder the movement of the dislocation, which leads to the pile-up of the Orowan loops and dislocations around the oxide particles with the increase of strain.

6. Conclusion

In the present work, the dislocation behavior and damage evolution of the irradiated ODS HEA are investigated using the random field theory-informed DDD simulation. The lattice distortion field in the developed model is derived from HRTEM experiments. The coupling interaction of the cutting and Orowan bypassing mechanism is for the first time introduced into DDD simulation, which is consistent with the recent experimental studies. A unique perfect dislocation loop annihilation is observed due to the multiple interactions between the edge dislocation and the dislocation loop. In addition, the damage evolution in ODS HEA decreases first and then increases with the strain, attributed to the irradiated dislocation loop annihilation and dislocation multiplication. With the increase of strain, the damage mechanism would be gradually shifted

from dislocation loop damage to strain localization damage. The distribution of the damage region is shifted from the random distribution to the concentration in the vicinity of the oxide particles. With the same irradiation condition and strain, the ODS HEA has a small damage region and a low damage degree compared with the HEA without oxide particles. These are the main causes: (1) The existence of the oxide particle impedes the dislocation slip and mass multiplication; (2) Oxide dispersion strengthening provides a high yield strength in the HEA; (3) The combined effect of the oxide particle and the lattice distortion leading to the annihilation of more dislocation loops and a low dislocation loop damage. This work sheds light on understanding the origin of strengthening and damage mechanism in the ODS HEAs, and then develops the novel material with the ultrahigh strength and low radiation damage for a wide application in an extreme environment.

Declaration of competing interest

The authors declare that they have no known competing financial interests or personal relationships that could have appeared to influence the work reported in this paper.

Acknowledgements

The authors would like to deeply appreciate the support from the National Natural Science Foundation of China (Nos. U2267252, 12372069, 12302083, and 12172123), the China Postdoctoral Science Foundation (No. 2023M731061), the Natural Science Foundation of Hunan Province (No. 2022JJ20001), and the Hunan Provincial Innovation Foundation for Postgraduate (No. CX20220378). Peter K Liaw very much appreciates the support from the National Science Foundation (Nos. DMR-1611180, 1809640, and 2226508).

Supplementary materials

Supplementary material associated with this article can be found, in the online version, at doi:10.1016/j.jmst.2024.02.017.

References

[1] Y. Chen, J. Lin, B. Jia, X. Wang, S. Jiang, T. Ma, Adv. Mater. 34 (2022) 2201796.
[2] Y.R. Lin, A. Bhattacharya, D. Chen, J.J. Kai, J. Henry, S.J. Zinkle, Acta Mater. 207 (2021) 116660.
[3] Z. Zakaria, S.K. Kamarudin, K.A. Abd Wahid, S.H.A. Hassan, Renew. Sust. Energ. Rev. 144 (2021) 110984.
[4] S.B. Bell, K.A. Kane, C.P. Massey, L.A. Baldesberger, D. Lutz, B.A. Pint, J. Nucl. Mater. 557 (2021) 153242.
[5] X. Xiao, D. Song, J. Xue, H. Chu, H. Duan, J. Mech. Phys. Solids 78 (2015) 1–16.
[6] Z. Zhang, Z. Su, B. Zhang, Q. Yu, J. Ding, T. Shi, E. Ma, Proc. Natl. Acad. Sci. U. S. A. 120 (2023) e2218673120.
[7] W. Wen, A. Kohnert, M.A. Kumar, L. Capolungo, C.N. Tomé, Int. J. Plast. 126 (2020) 102633.
[8] N. Castin, G. Bonny, A. Bakaev, F. Bergner, C. Domain, J.M. Hyde, L. Malerba, Mater. Today Energy 17 (2020) 100472.
[9] D. Manno, L. Torrisi, L. Silipigni, A. Buccolieri, M. Cutroneo, A. Torrisi, A. Serra, Appl. Surf. Sci. 586 (2022) 152789.
[10] L.J. Cui, H.L. Yang, Y.F. Du, Q.Q. Shi, S. Kano, H. Abe, J. Nucl. Mater. 569 (2022) 153920.
[11] K. Ma, B. Décamps, L. Huang, R.E. Schäublin, J.F. Löffler, A. Fraczkiewicz, M. Loyer-Prost, Acta Mater. 246 (2023) 118656.
[12] S. Chen, Z.H. Aitken, S. Pattamatta, Z. Wu, Z.G. Yu, D.J. Srolovitz, Y.W. Zhang, Nat. Commun. 12 (2021) 4953.
[13] J.B. Seol, W.S. Ko, S.S. Sohn, M.Y. Na, H.J. Chang, Y.U. Heo, H.S. Kim, Nat. Commun. 13 (2022) 6766.
[14] E. Mak, B. Yin, W.A. Curtin, A ductility criterion for bcc high entropy alloys, J. Mech. Phys. Solids 152 (2021) 104389.
[15] D. Hua, Q. Zhou, Y. Shi, S. Li, K. Hua, H. Wang, W. Liu, Int. J. Plast. 171 (2023) 103832.
[16] Y. Ren, Q. Zhou, D. Hua, Z. Huang, Y. Li, Q. Jia, W. Liu, Sci. Bull. 69 (2023) 227–236.
[17] L. Yang, H. Ge, J. Zhang, T. Xiong, Q. Jin, Y. Zhou, X. Ma, J. Mater. Sci. Technol. 35 (2019) 300–305.
[18] C. Lu, T. Yang, K. Jin, N. Gao, P. Xiu, Y. Zhang, L. Wang, Acta Mater. 127 (2017) 98–107.
[19] O. El-Atwani, N. Li, M. Li, A. Devaraj, J.K.S. Baldwin, M.M. Schneider, E. Martinez, Sci. Adv. 5 (2019) eaav2002.
[20] Y. Lu, H. Huang, X. Gao, C. Ren, J. Gao, H. Zhang, T. Li, J. Mater. Sci. Technol. 35 (2019) 369–373.
[21] Y. Chen, S. Wang, H. Feng, W. Li, B. Liu, J. Li, Q. Fang, Int. J. Plast. 162 (2023) 103497.
[22] Y. Lin, T. Yang, L. Lang, C. Shan, H. Deng, W. Hu, F. Gao, Acta Mater. 196 (2020) 133–143.
[23] S. Chung, B. Lee, S.Y. Lee, C. Do, H.J. Ryu, J. Mater. Sci. Technol. 85 (2021) 62–75.
[24] M. Li, Y. Guo, W. Li, Y. Zhang, Y. Chang, Mater. Sci. Eng. A 817 (2021) 141368.
[25] A.O. Moghaddam, A. Cabot, E.A. Trofimov, Int. J. Refract. Meth. 97 (2021) 105504.
[26] M. Šćepanović, V. de Castro, I. García-Cortés, F.J. Sánchez, T. Gigl, C. Hugenschmidt, T. Leguey, J. Nucl. Mater. 538 (2020) 152230.
[27] A. Fu, B. Liu, B. Liu, Y. Cao, J. Wang, T. Liao, Y. Liu, J. Mater. Sci. Technol. 152 (2023) 190–200.
[28] S. Mohan, R. Ramachandran, C. David, G. Amarendra, J. Alloy. Compd. 920 (2022) 165869.
[29] Z. Cheng, J. Sun, X. Gao, Y. Wang, J. Cui, T. Wang, H. Chang, J. Alloy. Compd. 930 (2023) 166768.
[30] V.N. Voyevodin, S.A. Karpov, G.D. Tolstolutskaya, M.A. Tikhonovsky, A.N. Velikodnyi, I.E. Kopanets, I.V. Kolodiy, Philos. Mag. 100 (2020) 822–836.
[31] M. Sadeghilaridjani, A. Ayyagari, S. Muskeri, V. Hasannaeimi, R. Salloom, W.Y. Chen, S. Mukherjee, J. Nucl. Mater. 529 (2020) 151955.
[32] D.J. Barton, B.C. Hornbuckle, K.A. Darling, L.N. Brewer, G.B. Thompson, Mater. Sci. Eng. A 811 (2021) 141027.
[33] Z. Dong, Z. Ma, L. Yu, Y. Liu, Nat. Commun. 12 (2021) 5052.
[34] S. Sisodia, N.J. Sai, K. Lu, F. Knöpfle, A. Zindal, J. Aktaa, A. Chauhan, Int. J. Fatigue 169 (2023) 107485.
[35] J. Du, S. Jiang, P. Cao, C. Xu, Y. Wu, H. Chen, Z. Lu, Nat. Mater. 22 (2023) 442–449.
[36] X. Mao, K.H. Oh, J. Jang, Mater. Charact. 117 (2016) 91–98.
[37] R. Singh, U. Prakash, D. Kumar, K. Laha, Mater. Charact. 189 (2022) 111936.
[38] T.X. Yang, P. Dou, P. Zhang, Y.C. Yang, J. Nucl. Mater. 576 (2023) 154259.
[39] K. Lu, A. Chauhan, D. Litvinov, M. Schneider, G. Laplanche, J. Aktaa, J. Mech. Phys. Solids 180 (2023) 105419.
[40] L. Wang, J. Ding, S. Chen, K. Jin, Q. Zhang, J. Cui, E. Ma, Nat. Mater. 22 (2023) 950–957.
[41] Q. Zhang, R. Huang, J. Jiang, T. Cao, Y. Zeng, J. Li, X. Li, J. Mech. Phys. Solids 162 (2022) 104853.
[42] Q. Fang, J. Peng, Y. Chen, L. Li, H. Feng, J. Li, P.K. Liaw, Mech. Mater. 155 (2021) 103744.
[43] Q. Zhao, Q. Zhu, Z. Zhang, X. Li, Q. Huang, W. Yang, H. Zhou, J. Mech. Phys. Solids 181 (2023) 105455.
[44] J. Li, Y. Chen, Q. He, X. Xu, H. Wang, C. Jiang, C.T. Liu, Proc. Natl. Acad. Sci. U. S. A. 119 (2022) e2200607119.
[45] D. Bamney, R. Reyes, L. Capolungo, D.E. Spearot, J. Mech. Phys. Solids 165 (2022) 104920.
[46] X. Guo, C. Sun, C. Wang, J. Jiang, M.W. Fu, Int. J. Plast. 145 (2021) 103076.
[47] A. Das, Scr. Mater. 218 (2022) 114833.
[48] Y. Shen, D.E. Spearot, Model Simul. Mater. Sci. 29 (2021) 085017.
[49] M. Li, X. Tian, W. Jiang, Q. Wang, H. Fan, J. Mech. Phys. Solids 173 (2023) 105238.
[50] R.B. Sills, N. Bertin, A. Aghaei, W. Cai, Phys. Rev. Lett. 121 (2018) 085501.
[51] W.C. Chang, Y.C. Lu, C.H. Hsueh, O, Mater. Sci. Eng. A 859 (2022) 144196.
[52] S. Lee, D. Chatain, C.H. Liebscher, G. Dehm, Scr. Mater. 203 (2021) 114044.
[53] Z. Lei, X. Liu, Y. Wu, H. Wang, S. Jiang, S. Wang, Z. Lu, Nature 563 (2018) 546–550.
[54] J.R.O. Leo, S.P. Barroso, M.E. Fitzpatrick, M. Wang, Z. Zhou, Mater. Sci. Eng. A 749 (2019) 158–165.
[55] A. Lehtinen, F. Granberg, L. Laurson, K. Nordlund, M.J. Alava, Phys. Rev. E 93 (2016) 013309.
[56] A. Lehtinen, L. Laurson, F. Granberg, K. Nordlund, M.J. Alava, Sci. Rep. 8 (2018) 6914.
[57] H. Salmenjoki, L. Laurson, M.J. Alava, Mater. Theory 4 (2020) 1–16.
[58] C. McElfresh, Y. Cui, S.L. Dudarev, G. Po, J. Marian, Int. J. Plast. 136 (2021) 102848.
[59] Y. Chen, Q. Fang, S. Luo, F. Liu, B. Liu, Y. Liu, J. Li, Int. J. Plast. 155 (2022) 103333.
[60] V. Mohles, Philos. Mag. A 81 (2001) 971–990.
[61] V. Skogvoll, L. Angheluta, A. Skaugen, M. Salvalaglio, J. Viñals, J. Mech. Phys. Solids 166 (2022) 104932.
[62] S. Peng, Z. Lu, L. Yu, J. Alloy. Compd. 861 (2021) 157940.
[63] S. Peng, Z. Lu, X. Li, L. Yu, J. Alloy. Compd. 924 (2022) 166518.
[64] M.R. He, S. Wang, K. Jin, H. Bei, K. Yasuda, S. Matsumura, K. Higashida, I.M. Robertson, Scr. Mater. 125 (2016) 5–9.
[65] A. Arsenlis, M. Rhee, G. Hommes, R. Cook, J. Marian, Acta Mater. 60 (2012) 3748–3757.
[66] Q. Zhou, D. Luo, D. Hua, W. Ye, S. Li, Q. Zou, H. Wang, Friction 10 (2022) 1913–1926.
[67] G. Mesmacque, S. Garcia, A. Amrouche, C. Rubio-Gonzalez, Int. J. Fatigue 27 (2005) 461–467.
[68] H. Wang, J. Liu, G. Wen, Y.M. Xie, Finite Eelem. Anal. Des. 171 (2020) 103376.

[69] N. Bertin, W. Cai, J. Mech. Phys. Solids 121 (2018) 133–146.
[70] W. Cai, A. Arsenlis, C.R. Weinberger, V.V. Bulatov, J. Mech. Phys. Solids 54 (2006) 561–587.
[71] S. Chatterjee, Y. Li, G. Po, Int. J. Plast. 145 (2021) 103062.
[72] J.K. Lee, Y.Y. Earmme, H.I. Aaronson, K.C. Russell, Metall. Trans. A 11 (1980) 1837–1847.
[73] R. Santos-Güemes, J. Segurado, J. LLorca, Eur. J. Mech. A-Solids 93 (2022) 104540.
[74] N.K. Kumar, C. Li, K.J. Leonard, H. Bei, S.J. Zinkle, Acta Mater. 113 (2016) 230–244.
[75] H. Ji, K. Ren, L. Ding, T. Wang, J.M. Li, J. Yang, Mater. Today Commun. 30 (2022) 103020.
[76] Y. Cui, N. Ghoniem, G. Po, J. Nucl. Mater. 546 (2021) 152746.
[77] F. Li, T. Liu, T. Wang, A. Wang, J. Wang, Y. Yang, J. Mech. Phys. Solids 132 (2019) 103681.
[78] J.W. Yeh, Science 374 (2021) 0940–0941.
[79] Z. Ma, G. Ran, X. Qiu, Y. Li, Y. Ding, R. Zhang, Huang X, J. Nucl. Mater. 563 (2022) 153645.
[80] D. Kaoumi, V. Jammot, J. Nucl. Mater. 523 (2019) 33–42.
[81] P. Agrawal, S. Karthikeyan, S.K. Makineni, B. Gault, D. Banerjee, Acta Mater. 222 (2022) 117436.
[82] Y. Cui, G. Po, N. Ghoniem, Acta Mater. 132 (2017) 285–297.
[83] Y. Xu, F.F. Worsnop, D. Dye, F.P. Dunne, J. Mech. Phys. Solids 179 (2023) 105384.
[84] Y. Wu, M. Jia, X. Gou, W. Xu, Int. J. Solids Struct. 269 (2023) 112183.
[85] Q. Gao, C. Jiang, H. Zhang, Q. Ma, H. Zhang, Z. Liu, H. Li, Mater. Sci. Eng. A 831 (2022) 142181.
[86] J. Wang, J. Chen, C. Guo, X. Xiao, H. Wang, B. Yang, Int. J. Fatigue 137 (2020) 105642.
[87] W. Liu, L. Chen, L. Yu, J. Fu, H. Duan, Int. J. Plast. 151 (2022) 103211.
[88] X. Lu, J. Zhao, C. Yu, Z. Li, Q. Kan, G. Kang, X. Zhang, J. Mech. Phys. Solids 142 (2020) 103971.
[89] A. Hunter, D.L. Preston, Int. J. Plast. 151 (2022) 103178.
[90] C. Ji, Y. Cui, Y. Li, N. Ghoniem, J. Mech. Phys. Solids 167 (2022) 105005.
[91] M. Rhee, H.M. Zbib, J.P. Hirth, H. Huang, T. De la Rubia, Model. Simul. Mater. Sci. Eng. 6 (1998) 467.
[92] K. Gururaj, C. Robertson, M. Fivel, Phil. Mag. 95 (2015) 1368–1389.
[93] Y. Wu, F. Zhang, X. Yuan, H. Huang, X. Wen, Y. Wang, Z. Lu, J. Mater. Sci. Technol. 62 (2021) 214–220.
[94] Q. Fang, W. Lu, Y. Chen, H. Feng, P.K. Liaw, J. Li, J. Mech. Phys. Solids 169 (2022) 105067.
[95] Y. Ijiri, N. Oono, S. Ukai, S. Ohtsuka, T. Kaito, Y. Matsukawa, Nucl. Mater. Energy 9 (2016) 378–382.
[96] K. Tsugawa, S. Hayakawa, Y. Iwase, T. Okita, K. Suzuki, M. Itakura, M. Aichi, Comput. Mater. Sci. 210 (2022) 111450.